Chapter 5
Flame Flashback in Supersonic Flows

Non-stationary flame propagation against the incoming supersonic flow in scramjet engines has been in focus of numerous experimental and computational studies. In this chapter, we give the research work of the flame flashback phenomenon in scramjet combustor under a condition of flight Mach 4 and Mach 5.5.

5.1 Flame Flashback Phenomenon in a Flight Mach 4 Condition

This part experimentally investigates the flame flashback in scramjet combustor with a cavity flameholder under a condition of flight Mach 4 adopted to gain additional insights into the driving mechanism of combustion instability in this special condition. Section 5.1.1 presents experimental investigation of flame flashback phenomenon and the calculated flashback flame speed. Section 5.1.2 presents the injection parametric study of flame flashback which includes fuel-equivalence ratio and injection schemes.

5.1.1 Flashback Flame in a Single-Side Expansion Scramjet Combustor

In scramjet combustors, Reynold's number is huge and the boundary layer is very thin. The high compressibility of supersonic flows suppresses the developments of instabilities. Under such conditions, the mechanism of flame propagation is still not clear, which concerns especially flame flashback against the supersonic flow. Wang et al. [1] have observed flame propagation against the incoming supersonic flow under certain mixing state with a fixed fuel equivalence ratio. In this part, Sun et al. [2] obtain strong variations the flame flashback parameters at various equivalence

M. Sun et al., *Unsteady Supersonic Combustion*,
https://doi.org/10.1007/978-981-15-3595-6_5

ratio in an ethylene-fueled model scramjet combustor with inflow $M = 2.1$ and stagnation temperature $T_0 = 846$ K, which simulates Mach 4 flight condition. The results obtained allow obtaining more efficient heat release in the scramjet.

5.1.1.1 Experimental Description

The model combustor shown in Fig. 5.1 has a total length of 2200 mm and consisted of one constant area section and three divergent sections with the expansion angles of 2.5°, 3.5°, and 4°, respectively. The entry cross section of the combustor is 54.5 mm in height and 75 mm in width. There is one cavity (denoted as 'T1') installation in the top wall of the test section. The distance from the cavity leading edge to the combustor inlet is 544 mm. The cavity depth is $D = 15$ mm, length to depth ratio $L/D = 7$, and the aft wall angle $A = 45°$. Figure 5.1 shows also the optional fuel injection locations: I1, I2 denote the injection locations set upstream with a distance of 250 mm and 260 mm to T1 cavity leading edge, respectively. The injector configuration (orifice number × diameter, 3 × 2.0 mm, the distance between the orifices is 15 mm) is conducted on a module which could be uninstalled. A high-frequency voltage signal corresponding to wall pressure change was acquired by a water-cooled high-frequency sensor (PCB model 112A05) at the point on the side wall where the location is 240 mm, 120 mm, 0 mm and −115 mm upstream of the T1 cavity leading edge respectively and 36 mm above the bottom wall (shown in Fig. 5.1). The acquisition frequency of the pressure signal is 50 kHz. The flowfield is visualized through two quartz window for high speed imaging camera with 8000 frames per second. The Schlieren system uses a laser light and the shutter time is 1/120,000 s. In the present work, the test facility has been operated twice for each scheme in Table 5.1 to allow comparison between the flame photos and the Schlieren images. The flow conditions of the scramjet combustor entry are $M = 2.1$ and stagnation temperature $T_0 = 846$ K, which simulates Mach 4 flight condition.

Table 5.1 shows the detailed injection schemes, where $\dot{m}_f$ represents the fuel mass flow rate and P_{0i} is the injection stagnation pressure. Schemes 1–5 were employed to compare the combustion instability features for injection with various fuelling rates and demonstrate different flame dynamics regimes. Ethylene was injected at the condition of stagnation temperature $T_{0i} = 300$ K. For Scheme 1, the flame quenches

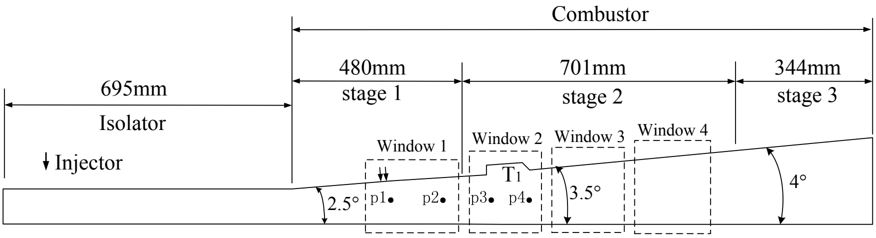

Fig. 5.1 Schematic of test section and cavity installation scheme [2]

Table 5.1 Injection schemes and flame dynamics phenomena [2]

	Injectors	P_{0i} (MPa)	$\dot{m}_f$ (g/s)	Flame dynamics
Scheme 1	$I_1 + I_2$	4.0	65.3	Extinction
Scheme 2	$I_1 + I_2$	3.0	55.0	Oscillating
Scheme 3	$I_1 + I_2$	2.0	39.5	Oscillating
Scheme 4	I_1	3.0	28.2	Oscillating
Scheme 5	I_1	2.0	19.1	Weak flame

immediately after forced-ignition is turned off; quenching happens due to the higher injection penetration, which causes little fuel entrained into the cavity shear layer and the flame cannot be stabilized. For Schemes 2–4, oscillating or fluctuating flames are obtained. For Scheme 5, we observe a weak flame in the T1 cavity. It is inferred from Table 5.1 that $\dot{m}_f$ plays an important role in the flame dynamics.

5.1.1.2 Results and Discussion

Figure 5.2 shows high-speed flame luminosity images of Scheme 2. The images demonstrate the details of the flame flashback (from T1 cavity to injection location) and flame blow-off. It is seen from Fig. 5.2a–c that, with support of the pilot flame in the cavity shear layer, explosive combustion develops the in supersonic flow downstream of the cavity. During this process the flame in the main flow becomes bright, which indicates considerable increase of the combustion intensity. At this stage the flame propagates against the incoming supersonic flow and spreads from the boundary layer to the bulk flow. In Fig. 5.2d–f, the flame base moves upstream of the cavity into the wake of the fuel jet very quickly until it goes through the jet injection location. In Fig. 5.2g–j, the flame quenches and is blown off downstream in a short time to the cavity location where flame is sustained again in the cavity shear layer. In Fig. 5.2k–i, burning stabilized in the cavity shear layer acts as a pilot flame, and reignites the bulk of the fuel/air mixture after certain time (about 1.9 ms averagely). From the Schlieren images in the first window, it is found that the pre-combustion shock train is pushed forward and the I1 and I2 injection has a higher penetration height during the flame flash-back. When a transient thermal throat is formed near the injection location, the fuel-air mixing is strongly enhanced and the combustion region transversely expands to the whole flow.

For Schemes 3 and 4, the flame stabilized in T1 cavity shear layer can flash back, while the leading flame is mostly stabilized in the I1 jet wakes and fluctuates intermittently within a short distance downstream of the I1 injector. The flame is not able to flash back through the jet injection location. For Scheme 5, a weak flame is always stabilized in the cavity shear layer and no flame flashback occurs in the whole procedure.

Figure 5.3 shows the measured pressure histories of different PCB sensors and the calculated flashback flame speed. The pressure signal of Scheme 2 has an intense

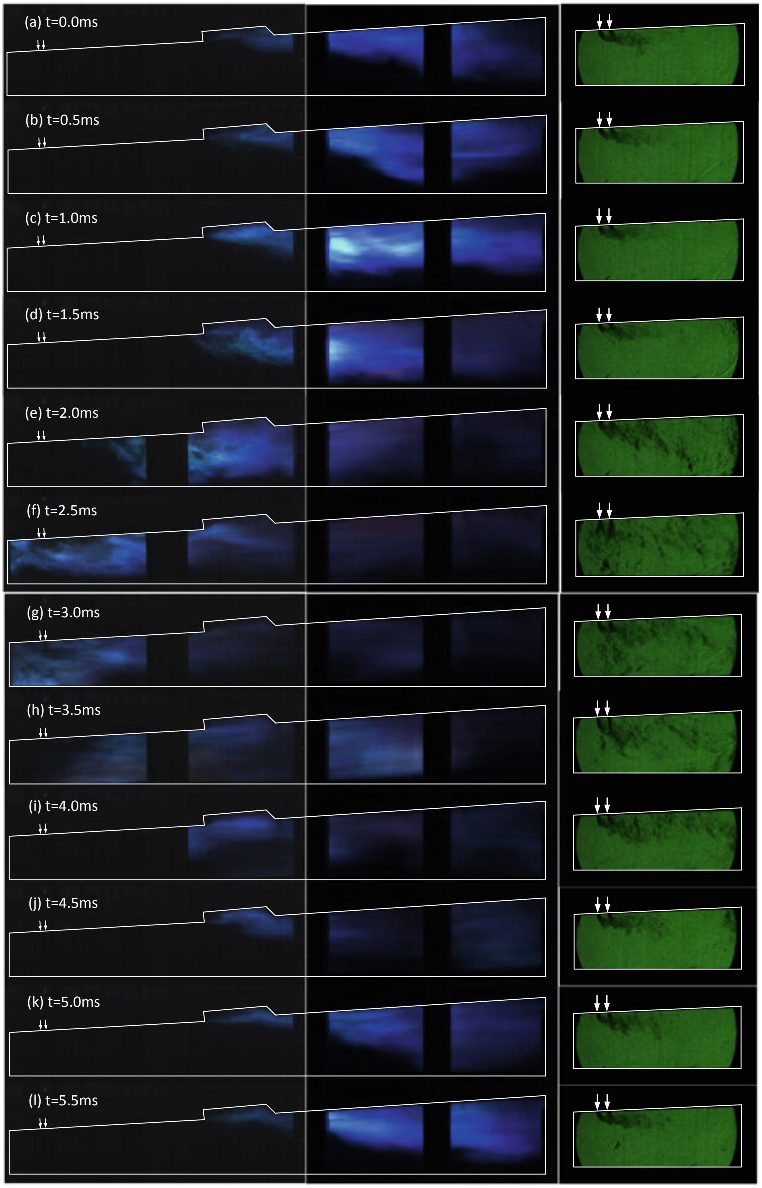

Fig. 5.2 Typical luminosity and schlieren movies of flame flash-back and blow-off event for scheme 2 (the left side are luminosity images and the right side are schlieren images) [2]

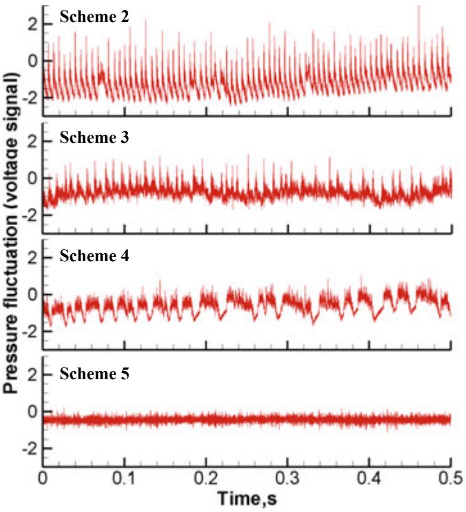

a) Histories of pressure signals of different schemes measured by PCB1

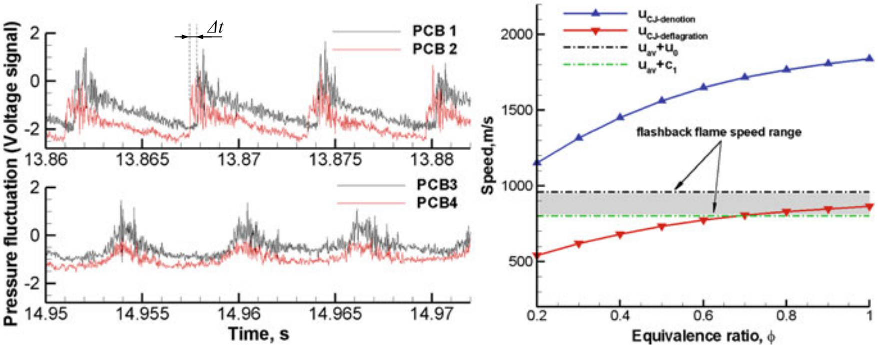

b) Pressure histories of PCBs 1-4 of Scheme 2

c) flashback flame speed range

Fig. 5.3 Pressure histories inside the combustor and the calculated flashback flame speed [2]

magnitude with transition between the pressure peak and the minimum point happening very quickly. For Scheme 4, an intermittent character of pressure pulsations is observed with much lower pulsation amplitudes as compared to Scheme 2. For Scheme 3, the oscillations develop in a hybrid mode of Schemes 2 and 4; in that case leading flame is stabilized in the I1 jet wakes at most of time, while intermittent pressure drops sporadically occur. Scheme 5 has the lowest pressure fluctuations among Schemes 2–5. During the flame flashback in Scheme 2, the shock movement ahead of the flame leads to a specific shape of the pressure signal in the oscillation period, with extremely sharp start and subsequent relaxation as shown in Fig. 5.3a. We believe that, as the equivalence ratio increases, the flame in the cavity T1 ignites the fuel/air mixture in the main stream and produces an intense heat release, which leads to explosive combustion. The unstable flame propagates through the premixed region, which increases considerably energy release in the process and, in turn, promotes fast flame propagation. For Scheme 4, the mixing equivalence ratio is lower and the ignition cannot produce an explosive combustion. Even if the flashbacks occur, the flame propagation cannot produce sufficient energy release in the process and the amplitude of flame oscillations remains moderate. In that case the flame front cannot go through the premixed region sufficiently fast, and the flame base remains stabilized in the low speed region of the jet-wake with a proper local equivalence ratio. In Scheme 4, the pressure drops are presumably related to large enough flow fluctuations able to extinguish the flame, which is then convected downstream to the cavity stabilized location. As the fuel equivalence ratio increases, the energy of the instantaneous heat release is increased too, and hence the amplitude of the flame flashback oscillations becomes larger.

As shown in Fig. 5.3b, the pressure peaks are recorded in sequence when the flame front or the leading shock passes by the PCB transducers. No obvious phase difference is observed for the peak pressure for PCB 3 and 4. However, the pressure peak of PCB 1 and 2 give obvious time shifts Δt, which means acceleration of the flamefront as well as increase in the propagation speed and amplitude of the leading shock. Here we remind that PCBs 3–4 are located in the downstream region and PCBs 1–2 are placed upstream of the cavity T1.

Since the flame is stabilized/propagates in the supersonic flow, the flame propagation speed with respect to the flow during the flash-back is comparable to the speed behind the oblique shock wave. Then the average flame speed relative to a fixed observer or walls is calculated as two instantaneous pressure peak signals, $u_{av} = \frac{1}{n}\sum_i^n \frac{\Delta L}{\Delta t_i}$, where n is the number of pressure peaks, ΔL is the distance between the two PCB transducers, and Δt_i is the time interval of two step signals shown in Fig. 5.3b. For Schemes 2–4, the flame speed relative to the walls is approximately 318.3 m/s, 218.2 m/s and 207.7 m/s, respectively. The shocks ahead of the flame are oblique instead of normal, and the flow velocity behind oblique shocks is somewhat higher than the local sound speed. Here we take the local sound speed c_1 as the lower limit to evaluate the flame speed, that is $u_{av} + c_1$. The upper limit of the flame speed relative to the walls is taken as $u_{av} + u_0$, where u_0 is the normal shock velocity relative to the incoming flow. Figure 5.3b shows the flame speed range and the respective speed for the Chapman–Jouguet (CJ) detonation and deflagration versus the ethylene-air equivalence ratio. The CJ deflagration speed relative to the walls is evaluated as [3, 4]

$$(u_{CJ})_{deflagration} \approx \frac{\gamma(\gamma-1)+2(\gamma+1)}{2(\gamma+1)^2}\sqrt{2\left(\gamma^2-1\right)Q} \tag{5.1}$$

where Q is the chemical energy release in the ethylene-air mixture and γ is the specific heat ratio.

As shown in Fig. 5.3c, the estimated flame speed range is well located in between the CJ detonation and deflagration speed, with much better correlation to the CJ deflagration regime. This correlation indicates that the observed flame flashback process in Schemes 2–4 has much in common with the final stages of deflagration-to-detonation transition (DDT) in channels, for which the quasi-stationary CJ deflagration accelerates due to explosive run-away just ahead of the front and goes over to CJ detonation [3, 4]. We infer that the observed flame flashback demonstrates also similar features with strong flame acceleration (FA) in a tube filled with premixed gas [5]. During the flame flashing back to the I1/I2 injectors, the energy release rate appears to be sufficiently high and generates explosive compression, resulting in fast flames propagating at speed exceeding the CJ deflagration speed relative to the incoming flow between PCB 1 and PCB 2, see Fig. 5.3c. Though flame acceleration is the initial and the most important part of DDT [3, 4], it does not necessarily mean that flame acceleration always leads to DDT. In the present experimental conditions, the DDT process is presumably moderated and interrupted when flame reach to the injectors by the insufficient mixing. For the present conditions, the distance between the I1/I2 injectors and the T1 cavity is not long enough to establish the run-up distance for detonation. The flame front cannot propagate upstream of the injectors, which hence leads to flame extinction and blow-off. Still, for Scheme 2, quasi-detonation may be expected with higher equivalence ratio.

For Scheme 3, the weak flame sustained in the cavity shear layer corresponds to the case of weak FA [5]. Due to the limited heat release, the flame is not able to generate strong compression and propagate backwards. Compared to Schemes 3–5, it can be inferred that there is a critical fuel mass flow rate between 19.1 and 28.2 g/s, for which the flame flash-back can occur.

5.1.2 Injection Parametric Study in a Single-Side Expansion Scramjet Combustor

In addition to observe the detailed transient process of the flame flashback in a single-side expansion scramjet combustor. Ouyang et al. [6] had carried out a series of comparative experiments on different conditions for the injection parametric study of combustion oscillation in a single-side expansion scramjet combustor with inflow $M = 2.1$ and stagnation temperature $T_0 = 947$ K, which simulates Mach 4 flight condition.

5.1.2.1 Experimental Description

The facility is composed of air heater, supersonic nozzle and scramjet combustor. The model scramjet combustor is directly mounted downstream the supersonic nozzle of the air heater which heats the air by means of air/ethanol/O_2 combustion. A weight sensor mounted on the forehead of the air heater was used to measure the facility thrust changes during the experiments [7]. This system yielded a maximum force reading of 10,000 N with an uncertainty of 0.5%. The flow conditions of the supersonic nozzle exit, that is the scramjet combustor entry, are listed in Table 5.2

Table 5.2 Flow conditions at the scramjet combustor entry [6]

Ma	P (kPa)	T (K)	P_0 (MPa)	T_0 (K)	Y_{O_2}
2.1	71	528	0.65	947	23.3%

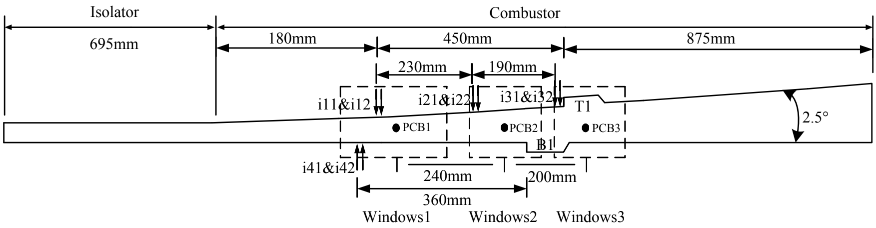

Fig. 5.4 Schematic diagram of the scramjet combustor model [6]

As Fig. 5.4 shows, the model scramjet combustor consists of a constant cross-section isolator and a single-side expansion combustor. The entry cross section of the combustor is 54.5 mm in height and 75 mm in width. The combustor has an expansion angle of 2.5° on the upside wall. The T1 cavity is arranged in the expansion-side wall (upside) and the B1 cavity is arranged in the straight-side wall (downside). The parameters of the cavities are set to depth $D = 15$ mm, length to depth ratio $L/D = 7$, and the aft wall angle $\mathrm{A} = 45°$. Figure 5.1 also shows the fuel injection locations. Four group injectors named i1, i2, i3 and i4 respectively, will be used in the experiments. Every group contains two rows injectors (orifice number × diameter, 3 × 2.0 mm in every row, the distance between the two rows is 15 mm), named im1 and im2, m denotes group name. The distance between groups is shown in Fig. 5.4.

The ethylene flame behavior is captured by a high speed movie camera through the three quartz windows on the model scramjet combustor, for which 4000 fps (frames per second) is chosen with a resolution of 1024 × 512 pixels and a shutter time of 1/5000 s. The flow structure is obtained with the schlieren system using a laser light and the shutter time is set 1/148,000 s with a frequency of 9300 fps. The pressures of combustor along the centerline of the upside wall in the test section are measured by a series of strain-gauge pressure transducers through taps with the diameter of 0.5 mm distributed on the upside wall. Furthermore, a high-frequency voltage signal corresponding to wall pressure change is acquired by a water-cooled high-frequency sensor (PCB model 112A05) at the points on the sidewall (shown in Fig. 5.4). The acquisition frequencies of the pressure signals are 50 kHz.

5.1.2.2 Effect of Fuel-Equivalence Ratio

In order to investigate the effect of equivalence ratio on the combustion oscillation in scramjet combustor,two group comparative experiments have been carried out which are listed in Table 5.3. The first group experiments are conducted when the

Table 5.3 Comparison experiments about effect of varying equivalence ratio [6]

Group no.	Scheme no.	Fuel	Injector	Cavity	Φ	Net thrust
1	Scheme 1	Ethylene	i11 + i12	T1	0.266	303
	Scheme 2				0.4	408
	Scheme 3				0.533	515
2	Scheme 4		i41 + i42	B1	0.266	Extinction
	Scheme 5				0.4	361
	Scheme 6				0.533	571

injectors and flame-holding cavity are mounted on the expansion-side wall (upside), and the second group on the straight-side wall (downside). The thrust increment of different schemes are also listed in Table 5.3, which is calculated from only the air heater working status to the scramjet engine plus air the heater working status [7]. The thrust increment can be used as one target parameter for the combustor performance assessment. Figure 5.5 shows the high-frequency pressure-time history of all available PCB transducers and for a detailed analysis of periodic characteristics, the frequency spectrum of all available PCB transducers is obtained using FFT (Fast Fourier Transform). The corresponding FFT transformed results are also displayed in Fig. 5.5.

Firstly, the results of first group experiments will be discussed. It can be found that when the global equivalence ratio is 0.266 (scheme 1), the irregularity of the pressure peak period is obvious, the combustion behaves as an intermittent oscillation. When the global equivalence ratio increases to 0.4 (scheme 2), however, the surprising change happens. The PCB results become regular and periodic, and it is easy to identify a clear principal frequency according to the frequency spectrum, which is about 126 Hz. The results when the global equivalence ratio is 0.533 (scheme 3) are analogous to scheme 2, its principal frequency is about 118 Hz. As the equivalence ratio is raised, the combustion oscillation becomes regular and its intensity becomes higher, mainly attributed to an increase in the combustion heat release, which can be validated by the net thrust in Table 5.3.

As to the second group results, when the global equivalence ratio is 0.266 (scheme 4), the flame cannot be hold and extinct, and when the global equivalence ratio is 0.4 (scheme 5), the result is analogous to scheme 1 instead of scheme 2, when the global equivalence ratio increases to 0.533 (scheme 6) in the end, the obvious periodic combustion oscillation achieved in the first group experiments cannot yet be observed, but the combustion oscillation is more frequent than scheme 5.

Comparing the two group experiments, we can found some similar and different results. The similar results contain two sides. On the one hand, as the global equivalence ratio increases, the combustion oscillation becomes more regular and frequent. It implies that the local thermal choking should be responsible for the combustion oscillation process. As Fig. 5.6 shows, the cavity-hold flame will be strengthened and expand transversely to the main flow before upstream propagation, and the ensuing flame upstream propagation exists in the bulk of flowpath instead of the vicinity of

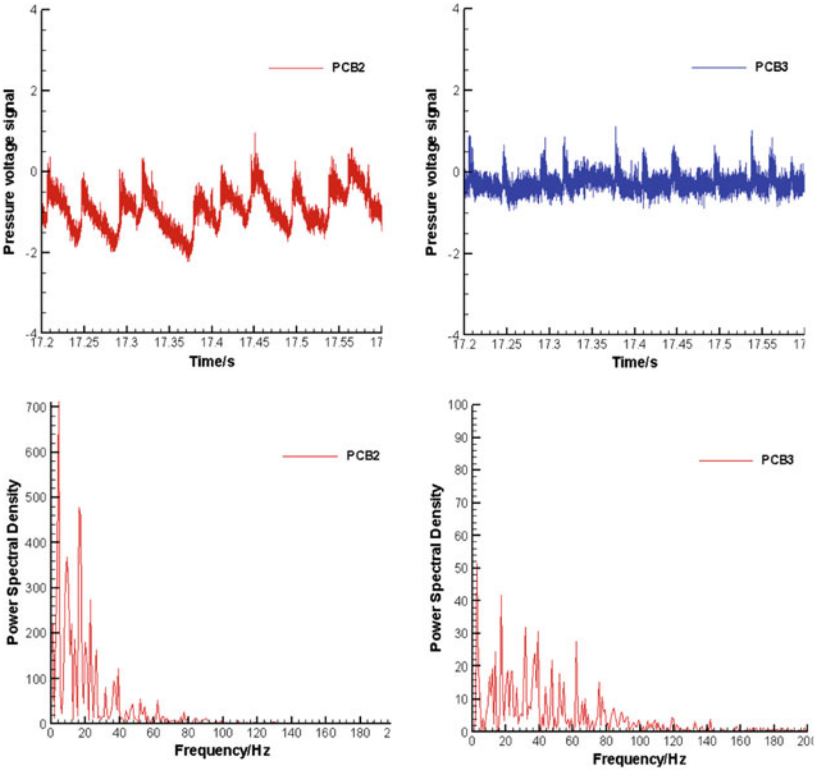

(a) scheme 1

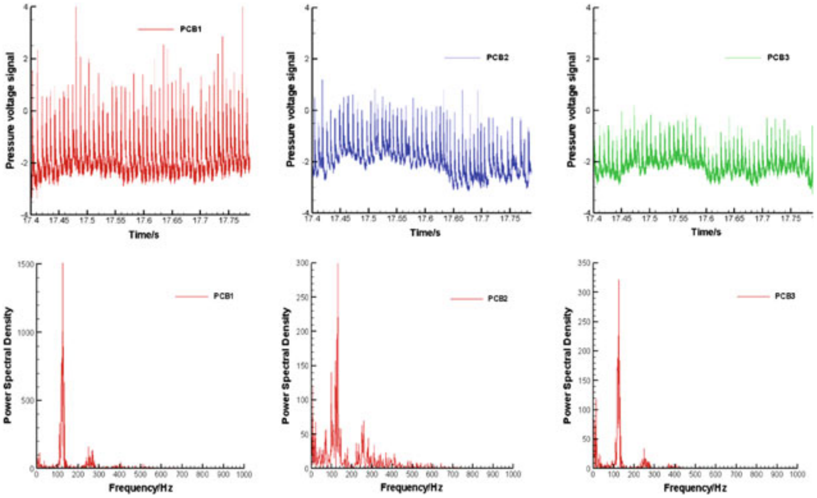

(b) scheme 2

Fig. 5.5 Histories and power spectra of high-frequency pressure signal of scheme 1–3, 5–6 [6]

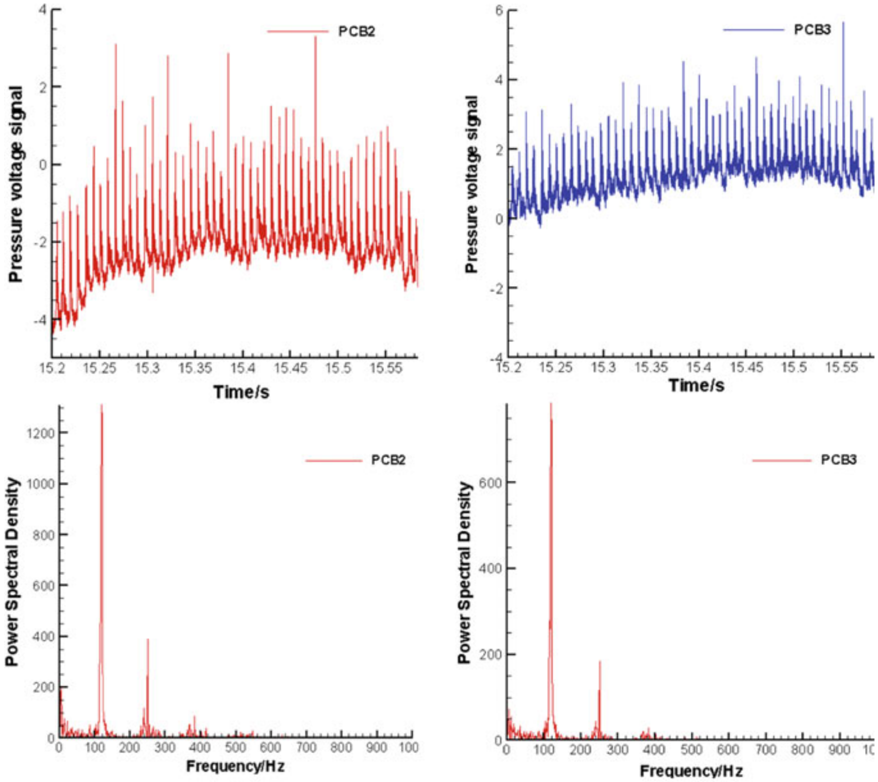

(c) scheme 3

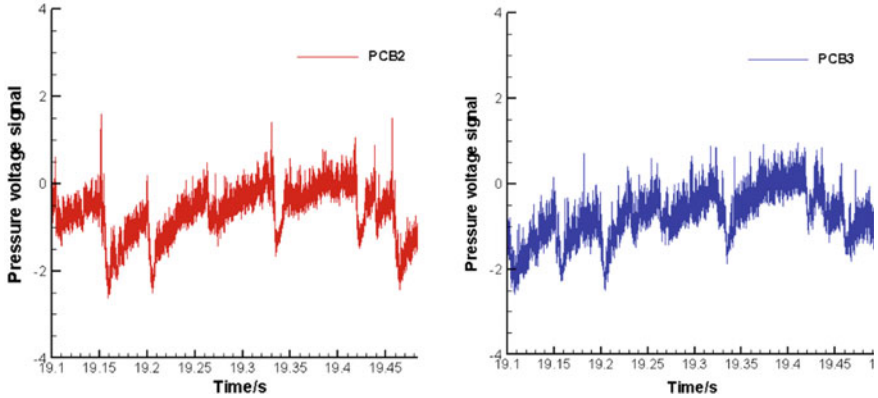

Fig. 5.5 (continued)

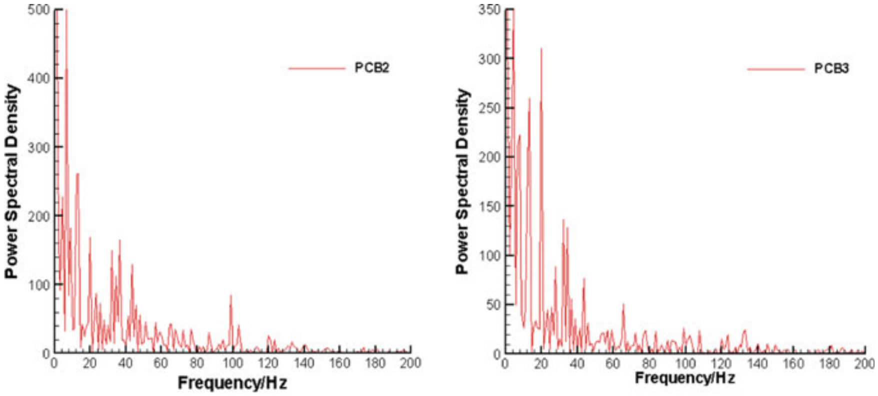

(d) scheme 5

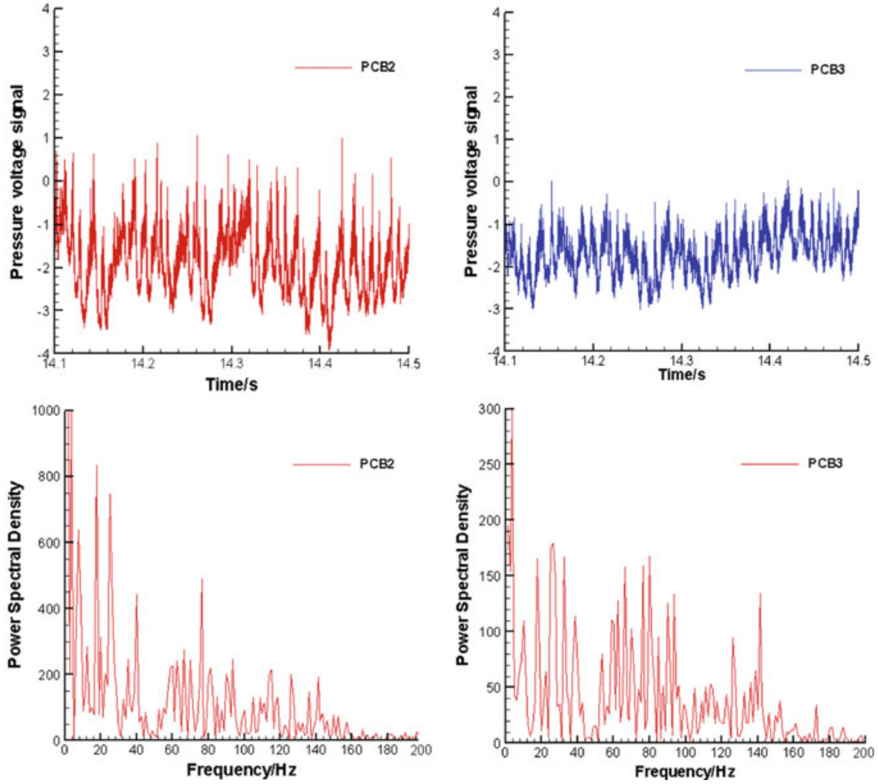

(e) scheme 6

Fig. 5.5 (continued)

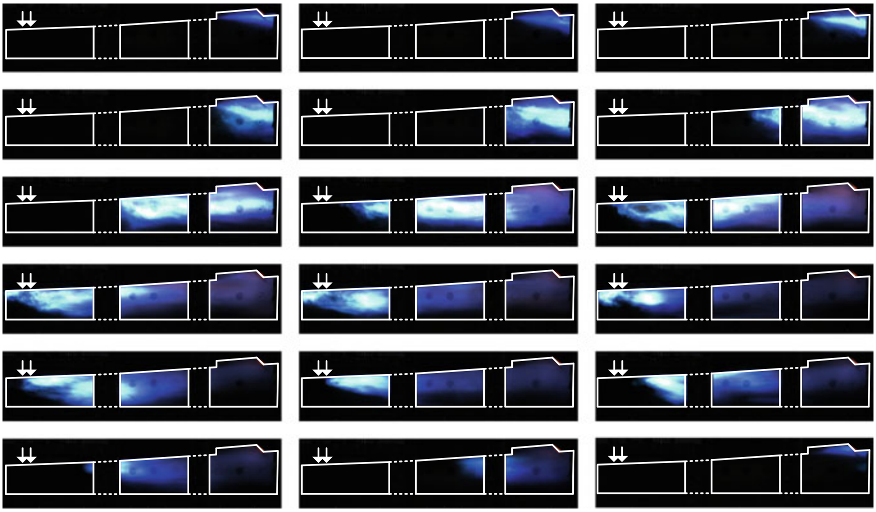

Fig. 5.6 Flame frames of one typical oscillation period in scheme 2. Time between images: 1/2000 s. Figure must be read from left to right and then, top to bottom [6]

wall. On the other hand, the combustion oscillation in the vicinity of the upstream PCB transducers is more intense at all global equivalence ratios which maybe be attributed to the intensive interaction between jet and combustion, which is shown as Fig. 5.7. The different result can be summarized that the regular and periodic

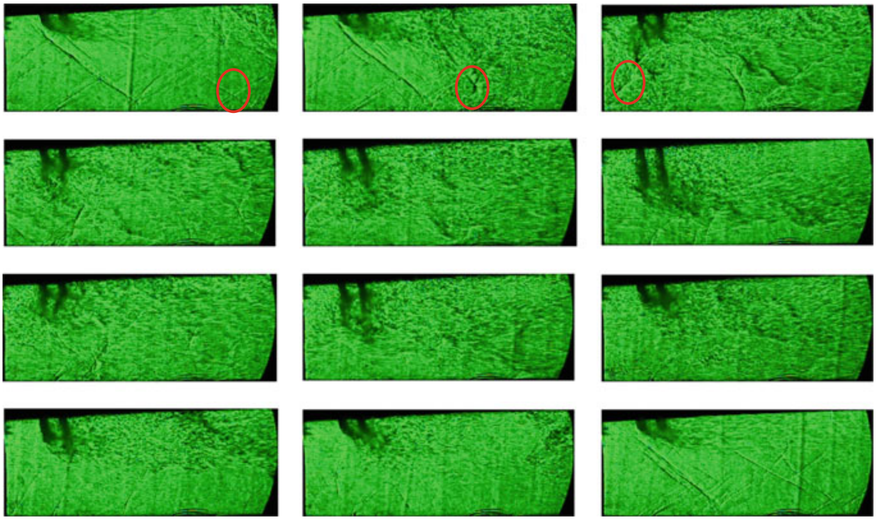

Fig. 5.7 Schlieren images of one typical oscillation period in scheme 2. Time between images: 3/3100 s. Figure must be read from left to right and then, top to bottom [6]

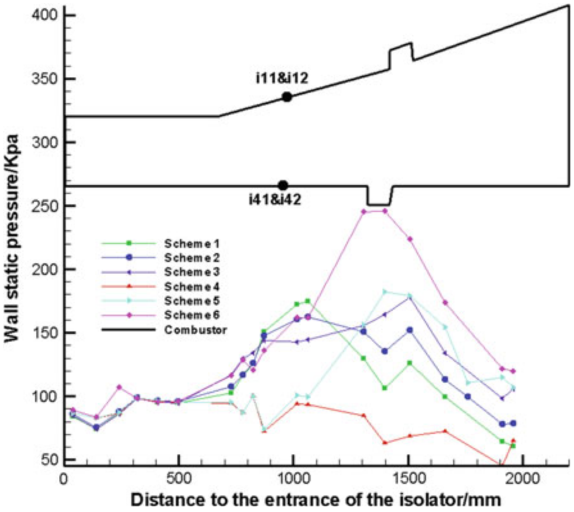

Fig. 5.8 Comparison of wall static pressure of scheme 1–6 [6]

combustion oscillation is more possible when the injectors and flame-holding cavity are mounted on the expansion-side wall (upside). This difference is related to the formation of the low-speed separation zone. Figure 5.8 shows the time-averaged upside static pressure of the six schemes. It can be found that when the injectors and flame-holding cavity are mounted on the expansion-side wall (upside), the main combustion heat zone is between injectors and cavity. However, when the injectors and flame-holding cavity are mounted on the straight-side wall (downside), the main combustion heat zone concentrates in the vicinity of cavity even the flame cannot be hold, which means the low-speed separation zone in front of cavity B1 has been suppressed, which can be deduced from Fig. 5.9. In Fig. 5.9, the injecting bow shock and its reflect shock exist most of the time, which indicates the flowfield maintain supersonic, so the improvement of the fuel jet penetration characteristic is not obvious. However, most of the flowfield in Fig. 5.7 is decelerated to subsonic when the flame upstream propagates to the vicinity of the fuel jet, which is identified by the disappearance of the injecting bow shock and its reflect shock. As Fig. 5.7 shows, it even can deflect towards incoming flow, which means that the flow or combustion instability reaches sufficient amplitude, and reversal of the flow occur which results in the low-speed separation zone spreads to the upstream of the injectors. Compared the shockwave structures in Figs. 5.7 and 5.9 carefully, some surprised difference can be find. In Fig. 5.7, as the flame propagates upstream, the pre-combustion shock wave (which has been marked with red ellipse in Fig. 5.7) appears close to downside, which will be strengthened and pushed upstream subsequently. This indicates that the flame upstream propagation should be attributed to the downstream thermal choking, which is in line with the standpoint of Laurence et al. [8–13]. As Fig. 5.9 shows, however, when the injectors and flame-holding cavity are mounted on the straight-side wall (downside), as flame propagate upstream, the boundary layer separation shock (which has been marked with white ellipse in Fig. 5.9) instead of the

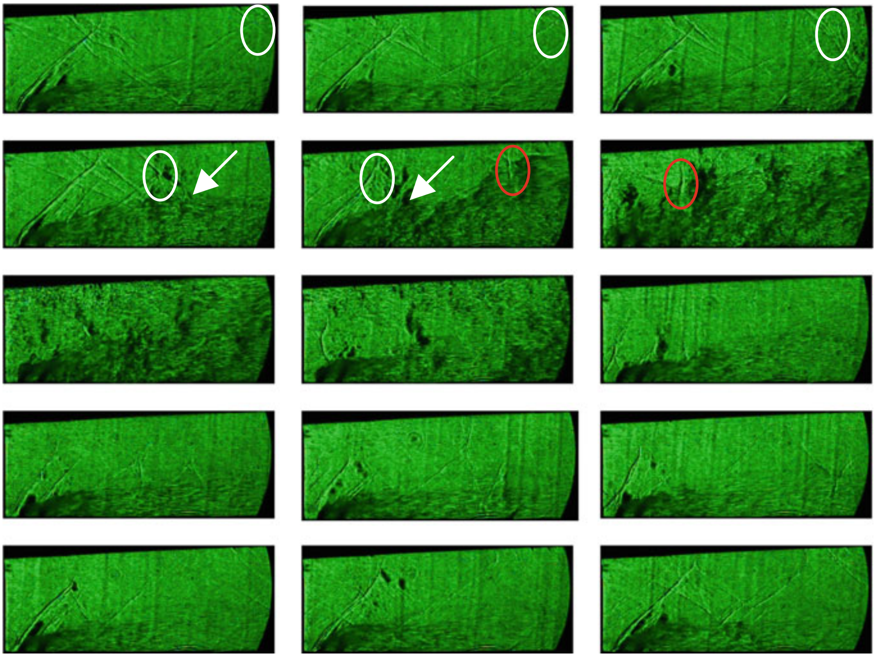

Fig. 5.9 Schlieren images of one typical oscillation period in scheme 5. Time between images: 3/3100 s. Figure must be read from left to right and then, top to bottom [6]

pre-combustion shock wave will appear close to upside, which will be strengthened and pushed to fuel jet subsequently. The strengthened separation shock will act on the fuel jet. The action will expand the jet wake, thus improve the penetration and mixing effect notably, which has been pointed out by the white arrowhead in Fig. 5.9. Subsequently, the improved mixing fuel will promote the downstream combustion and result in the pre-combustion shock wave (which has been marked with red ellipse in Fig. 5.9). The promoted combustion will only cause transient local thermal choking, which can be revealed by the successive schlieren images in Fig. 5.9. Unlike Fig. 5.7, in this operating condition, the flame upstream propagation should result from the boundary layer separation, which is corresponding to the perspective of Frost et al. [14–16]. The different mechanisms of flame upstream propagation lead to the different combustion oscillation characteristics, as the PCB results in Fig. 5.5 shows.

5.1.2.3 Effect of Injection Schemes

The former numerical study [17] has indicated that fuel injection scheme has important influence on ethylene reacting flowfiled. So it is necessary to investigate the influence of injection scheme on the combustion oscillation in scramjet combustor. Six comparative experiments have been considered in this investigation, as shown

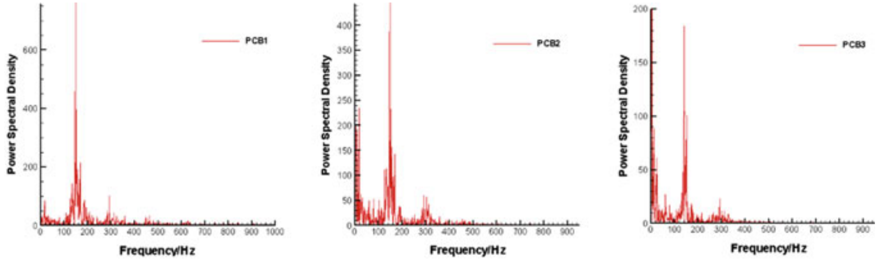

(a) scheme 7

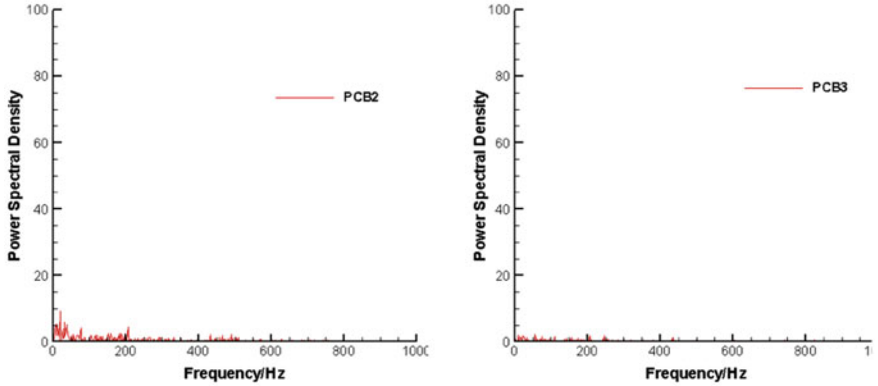

(b) scheme 9

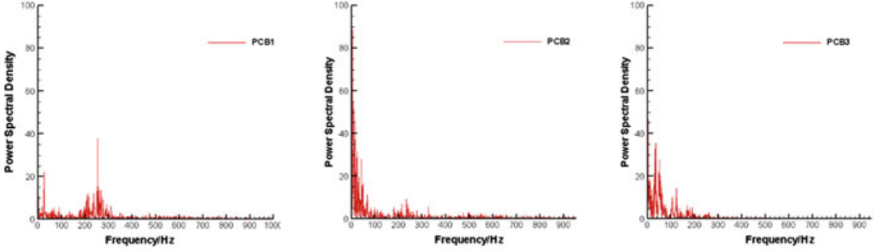

(c) scheme 10

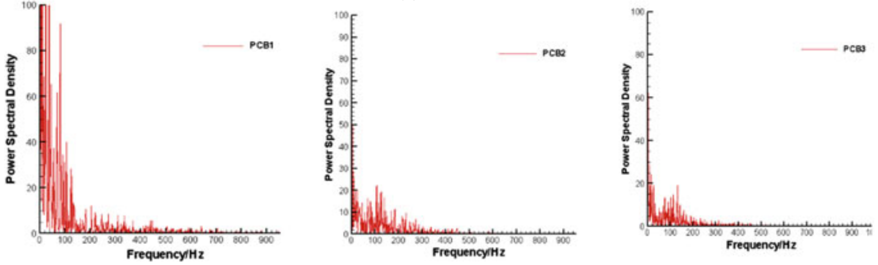

(d) scheme 11

Fig. 5.10 Power spectra of pressure signal of scheme 7, 9–11 [6]

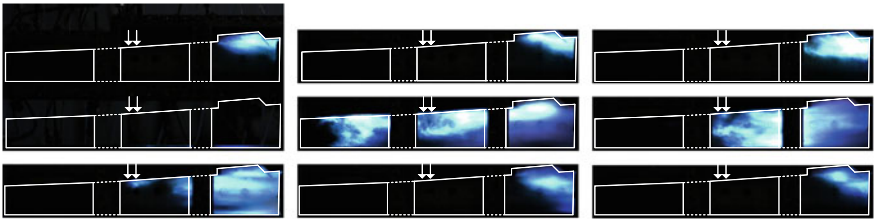

Fig. 5.11 Flame frames of one typical oscillation period in scheme 7. Time between images: 3/4000 s. Figure must be read from left to right and then, top to bottom [6]

Table 5.4 Comparison experiments about effect of varying injection schemes [6]

Group no.	Scheme no.	Fuel	Injectors	Cavity	Φ	Net thrust
Group 1	Scheme 2	Ethylene	i11 + i12	T1	0.4	408
	Scheme 7		i21 + i22			374
	Scheme 8		i31 + i32			Extinction
Group 2	Scheme 9		i11 + i31			286
	Scheme 10		i21 + i31			256
	Scheme 11		i11 + i21			394

in Table 5.4. The group 1 can be considered as centralized injection and group 2 as distributed injection. The thrust increment of different schemes is listed in Table 5.4, and for brevity, the PCB results are omitted in this section.

The result of group 1 shows that as the injectors are installed more closely to the inlet, the thrust increment become more remarkable. That is to say, increasing premixing distance will improve ethylene combustion characteristic. According to the FFT and flame results, however, we can found that the centralized injection will result in combustion oscillation in scramjet combustor. The principal frequency is about 150 Hz in scheme 7, which is higher than that of scheme 2, but its intensity of the FFT signal is lower. It indicates that although the longer premixing distance can increase thrust, it will increase the oscillation period and intensity. The extinction of scheme 8 may be not only because of the lacking of premixing but also the combustion oscillation, which reveals that the combustion oscillation in scramjet combustor can cause working uncertainty and instability. Thus, in order to avoid the combustion oscillation, the distributed injection in group 2 is considered. The intensity of the FFT signal of group 2 is lower than that of group 1 and the intensity of the FFT signal of case 9 is the lowest, which indicate that increasing the streamwise distance between injectors can relieve the combustion oscillation in scramjet combustor. Fig. 5.10 shows the comparison of combustion oscillations between the two injection schemes, and Fig. 5.11 shows one typical flame oscillation period of the distributed injection. As Fig. 5.12 shows, the separation of injectors will divide the flame into two parts, the upstream part and downstream part. It can be inferred that the insufficiently combustion hot products in upstream act as the plot flame of the downstream combustion, and thus the downstream combustion will result in sufficient adverse

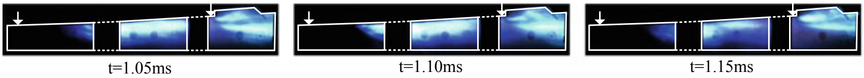

(a) scheme 9

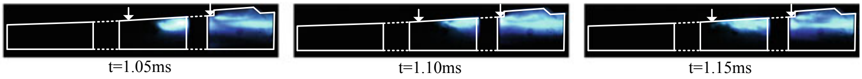

(b) scheme 10

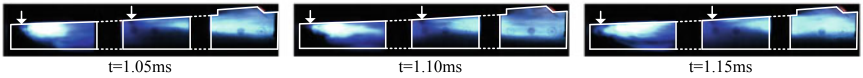

(c) scheme 11

Fig. 5.12 Flame frames of scheme 9–11 [6]

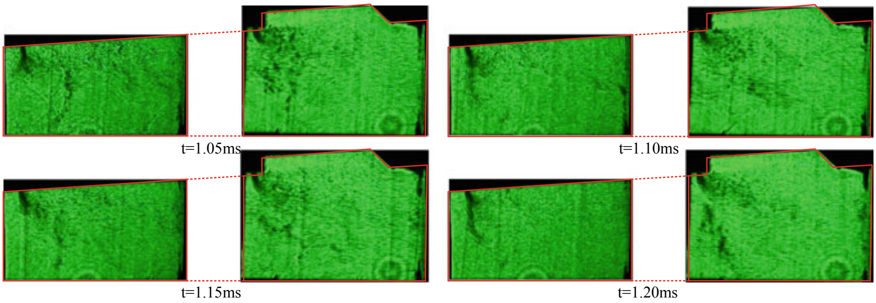

Fig. 5.13 Schlieren images of scheme 10 [6]

pressure gradient and cause local thermal choking, which can contribute to the stability of low-speed separation zone as Fig. 5.13 shows in which the injecting bow shock and its reflect shock is not visible through the observation windows. Thus, the stabilized divided flame has formed. Unlike the distributed injection, as Fig. 5.11 shows, the centralized injection will cause the generation and disappearance of low-speed separation zone periodically, which will result in combustion oscillation. According to the comparison between group 1 and group 2, it can be found that the distributed injection can avoid the combustion oscillation effectively as shown in Fig. 5.10.

5.2 Flame Flashback Phenomenon in a Flight Mach 5.5 Condition

This part experimentally investigates the combustion oscillation in scramjet combustor with a cavity flameholder under a condition of flight Mach 5.5. Especially, a combined numerical, and theoretical approach is adopted to gain additional insights into the driving mechanism of combustion instability in this special condition. The subchapter is organized as follows. Section 5.2.1 presents experimental investigation of flame flashback phenomenon. Section 5.2.2 presents numerical models and discusses the influencing factors of flame flashback, such as the boundary-layer effects, thermal disturbance, or local mixing degree. Section 5.2.3 introduces a simplified combustion opening system model to illustrate flame flashback mechanisms. In addition, a theoretical analysis model of the auto-ignition was established to investigate whether there is auto-ignition behaviour.

5.2.1 Experimental Investigations on Flame Flashback

Supersonic flame flashback is an important sub-process in the combustion oscillation process. Although flame flashback has been demonstrated in many experiments, the academic community has not yet reached a unified understanding of the exact factors that cause supersonic flame flashback. In order to improve the combustion efficiency of the scramjet engine while taking into account the reliability and robustness of the combustion chamber, this chapter uses the high-speed photography and schlieren technology, combined with the quantitative analysis method to simulate the flashback dynamic process and triggering factors in the combustion chamber of the scramjet engine. Systematic experimental studies, from injection parameter changes (total fuel equivalent ratio, fuel premixing distance, nozzle angle of incidence and number of nozzles) and cavity parameters (cavity length to depth ratio, cavity trailing edge inclination and cavity downstream air Throttling) two major aspects of discussion.

5.2.1.1 Experimental Description

The experiments are carried out in a direct-connected test facility, as detailed by Wang et al. [18], which is composed of an air heater, a supersonic nozzle, and a scramjet combustor. The air heater burns continuously pure ethyl alcohol and oxygen, and heats the gas to imitate flight Mach 5.5 conditions. As a result, we obtained a Mach 2.52 flow at the combustor entrance with a mass flux of about 1 kg/s. The detailed operation status at the nozzle and fuel injection are listed in Table 5.5. Ethylene is injected at the condition of stagnation temperature $T_0 = 300\,\mathrm{K}$ and stagnation pressure $P_0 = 2.1, 2.4, 2.7\,\mathrm{MPa}$, respectively. The corresponding

Table 5.5 Experimental conditions

Parameter	T_0 (K)	P_0 (MPa)	Ma	Y_{O_2} (%)	Y_{H_2O} (%)	Y_{CO_2} (%)	Y_{N_2} (%)	$Y_{C_2H_4}$ (%)
Air	1480	1.6	2.52	23.38	6.22	10.16	60.24	0.0
f_1/f_2 jet	300	2.1/2.4/2.7	1.0	0.0	0.0	0.0	0.0	100.0

global equivalence ratio, $\phi = 0.28, 0.34, 0.37$. The fuel–air equivalence ratio of a system is defined as the ratio of the fuel-to-oxidizer ratio to the stoichiometric fuel-to-oxidizer ratio. Mathematically,

$$\phi = \frac{m_{C_2H_4}/m_{O_2}}{\left(m_{C_2H_4}/m_{O_2}\right)_{st}} \tag{5.2}$$

where, m represents the mass, suffix st stands for stoichiometric conditions. It is important to note that the local equivalence ratios in the field near the upper wall are higher since only the upper wall injection is conducted. Local equivalence ratios in the field near the upper wall are higher since only the upper wall injection is conducted.

Figure 5.14 shows a schematic of the test section. A constant 200 mm long isolator is directly connected to the 40 mm high and 50 mm wide nozzle exit, followed by the 680 mm long test section consisting of a constant area section and a diverging section with expansion angle of 10°. A cavity ‘T_1’ is located on the top wall 220 mm downstream of the combustor entrance. The cavity is $D = 12$ mm in depth, $L = 56$ mm in length, with the aft wall angle $\theta = 45°$. Two pair fuel injectors (f1/f2) are fixed $L_1 + L_2$ mm and L_2 mm upstream of the cavity leading edge, respectively. Unless specified, L_1 equals 20 mm and L_2 equals 150 mm; each of injectors has 3 orifices at an angle of φ to the wall; each orifice is 1.0 mm in diameter with 10 mm interval distance in the transverse direction. To maintain a total constant jet area, the equivalent injector diameter of dual-jet case is 1.7 mm. A spark plug is fixed on the cavity floor to assist ignition. Its supply voltage is 220 V; however, the instantaneous discharge voltage is nearly 2000 V. The spark rate is 100 Hz.

The flow field is visualized by high speed imaging camera and schlieren system, through the quartz window which is 140 mm × 60 mm for photograph camera and schlieren observation. The schlieren system utilizes the semiconductor continuous laser as light source. The wavelength of the laser is 532 nm. To eliminate the influence of combustion radiation, a 532 nm single pass filter is installed in front of the image recorder. To observe the flame dynamics, the high-speed imaging and schlieren image

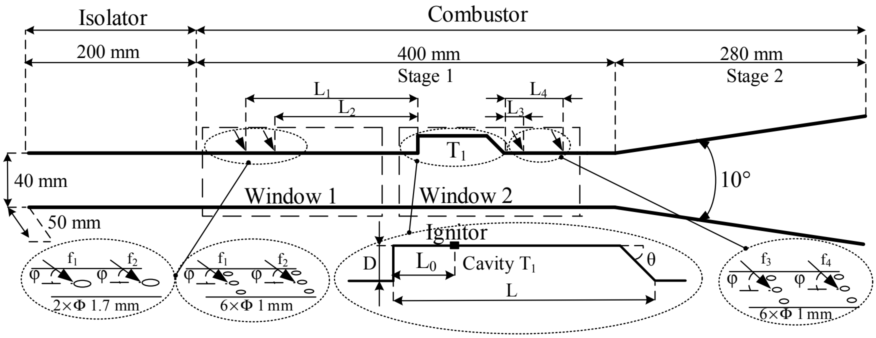

Fig. 5.14 Schematic diagram of test section and zoom diagram of injector and cavity

Table 5.6 Comparative experiments of the influence of injection parameters

Case	Total injection pressure/fuel-equivalence ratio	f_1 and f_2 injector	Outcome
1	$P_{jet} = 2.1$ MPa/$\Phi = 0.28$	$\varphi = 60°$ $L_2 = 150$ mm	Stable combustion
2	$P_{jet} = 2.4$ MPa/$\Phi = 0.34$	$\varphi = 60°$ $L_2 = 150$ mm	Periodic oscillation
3	$P_{jet} = 2.7$ MPa/$\Phi = 0.37$	$\varphi = 60°$ $L_2 = 150$ mm	Periodic oscillation with inlet unstart
4	$P_{jet} = 2.1$ MPa/$\Phi = 0.28$	$\varphi = 90°$ $L_2 = 150$ mm	Periodic oscillation
5	$P_{jet} = 2.1$ MPa/$\Phi = 0.28$	$\varphi = 90°$ $L_2 = 110$ mm	Periodic oscillation
6	$P_{jet} = 2.1$ MPa/$\Phi = 0.28$	$\varphi = 120°$ $L_2 = 110$ mm	Periodic oscillation
7	$P_{jet} = 2.7$ MPa/$\Phi = 0.37$	Dual-jet $\varphi = 60°$ $L_2 = 170$ mm	Stable combustion

cameras are set with 10000 fps (frames per second) 1024 × 256 pixels and shutter time of 1/25000 s. A pressure scanner is introduced to obtain the pressure along the combustor centerline of the top wall in the test section through taps with 1.0 mm diameter. The acquisition frequency of the pressure scanner is 100 Hz, with 0.25% full scale accuracy. The repeatability of the experimental procedure has been validated using numerous experiments [18–20].

5.2.1.2 Effect of Injection Parameters

The effects of equivalence-ratio, injection angle, and jets number on combustion oscillation phenomenon are investigated. The detailed flow conditions and outcomes are listed in Table 5.6.

Figure 5.15 shows the average pressure distribution along the model combustor upper wall. There are no combustion oscillation phenomena in cases 1 and 7, only stable flames anchored at the cavity. The combustions are concentrated mainly in the cavity and the boundary layer downstream of the cavity, with a peak pressure of about 240 kPa. In contrast, combustion oscillation occurs in other cases. As expected in case 3, the higher equivalence ratio causes the pressure profiles to increase. Violent combustion leads to increased pressure in isolator which leads to inlet unstart. But the pressure decreases in the cavity and downstream of the cavity, which indicates that the combustion is subsonic. For the rest cases, it is seen that the isolators almost keep the flow steady, and pressure fluctuations only start at the fourth measurement point. Due to the moderate combustion, the pressure decreases in the cavity and downstream of the cavity, with the peak pressure corresponding to about 350 kPa. Scram-ram transition occurs in types of periodic oscillation cases, when the pressure profile abruptly increases from stable combustion case (scram) to periodic oscillation with inlet unstart case (ram).

The effect of fuel-equivalence ratio

Firstly, the influence of injection pressure (or the global equivalence ratio) has been studied by the comparative experiments listed in Table 5.7. It should be noted that

Fig. 5.15 Wall pressure distribution for different cases along the upper wall

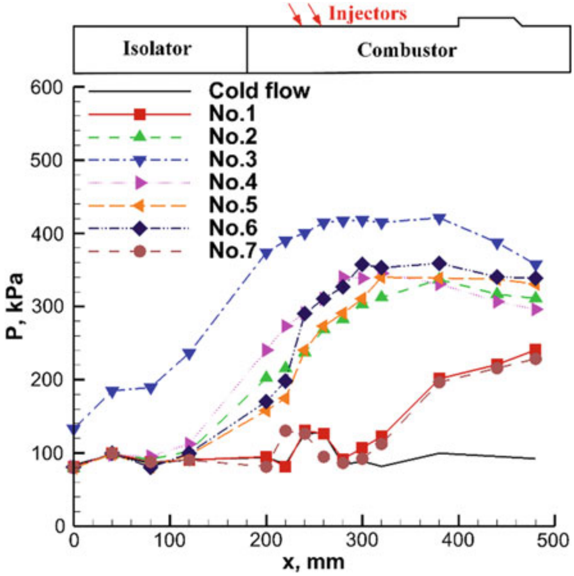

Table 5.7 Comparative experiments of the influence of global equivalence-ratio

Case	Total injection pressure/fuel-equivalence ratio	f_1 and f_2 injector	Outcome
1	$P_{jet} = 2.1$ MPa/$\Phi = 0.28$	$\varphi = 60°$ $L_2 = 130$ mm	Stable combustion
2	$P_{jet} = 2.4$ MPa/$\Phi = 0.34$	$\varphi = 60°$ $L_2 = 130$ mm	Periodic oscillation
3	$P_{jet} = 2.7$ MPa/$\Phi = 0.37$	$\varphi = 60°$ $L_2 = 130$ mm	Periodic oscillation with inlet unstart

the dark shadow between two quartz glass windows is the supporting structure of test section. As Fig. 5.16 shows, the pressure of injection is too weak to yield a high global equivalence ratio, the lower equivalence ratio cannot produce an explosive combustion in the premixed region. Hence, there is no combustion oscillation. In addition, the injection bow shock and its reflect shock exist all the time, which indicates the flow field maintains supersonic. The separated boundary layer is too thin to hold flame. Hence, the flame is stable in cavity shear layer.

Figure 5.17 shows the combustion oscillation for case 2, it can be seen that the large-amplitude combustion oscillation can be divided into three distinctive stages consisting of flame flashback, flame blown off, and flame re-holding. Compared with case 1, the higher injection pressure leads to the much more fuel injection and higher global equivalence, and more intense combustion occurs in the cavity and downstream boundary layer. By accumulating the energy from the exothermic reactions, the combustion intensity in the separated boundary layer is gradually enhanced. When energy exceeds a certain threshold level, the separated boundary full of flames occupies the flow channel. Then, the flame begins to propagate from the leading edge of the

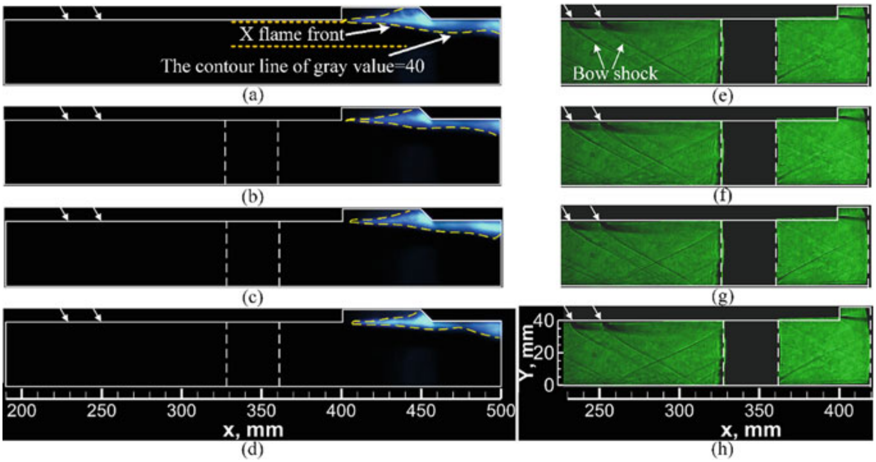

Fig. 5.16 Luminosity and schlieren visualizations of stable combustion for low equivalence-ratio. The time interval between two consecutive images is 1 ms [21]

cavity wall to the fuel injectors. As schlieren images show (Fig. 5.17i–l), the oblique shocks created by the impingement of the fuel injection are compressed and become a set of shock trains. The presence of shock trains indicates that thermal choking has occurred. Sharing the same standpoint with Laurence et al. [11, 13, 22], the thermal choking is the necessary condition of the flashback, and it results in large low-speed separation zone which plays a crucial role in the stability of flame combustion and in the enhancement of the combustion intensity. Along with more combustion heat-release going into heating the air flow, the pre-combustion shock trains near the fuel injector are gradually pushed forward, accompanying with enhancement of combustion. During the flame flashback process, the shock waves confine a high-pressure, high-temperature, low-speed region. The increased residence time promotes fuel mixing, thus enhancing combustion. It is also clearly seen in schlieren images that the low-speed promotes deeper jet penetration depth. All these effects lead to higher combustion intensity downstream of the cavity. The increased heat release rate forces the flame to propagate upstream, and the strengthened pre-combustion shock trains are subsequently pushed upstream. The flame core moves upstream very rapidly along the combustor wall, until it reaches the fuel injector locations.

After this stage, due to the lack of the fuel premixing effect, the local equivalence ratio is lost. Hence, the flame surrounding the injector cannot be sustained, and it is blown quickly back to the cavity. The flame then is re-stabilized in the rear of the cavity and the cavity shear layer, forming the cavity stabilized mode flame again. According to the corresponding schlieren images (Fig. 5.17m–p), the bulk flow is subsonic during most of this stage, and then recovers to supersonic, once the separation zone is pushed downstream owing to lack of heat release blockage. At the end of this stage, the bow shock (at the upper wall) re-appears upstream, and the flame is held in the cavity shear layer again, preparing for triggering of the next

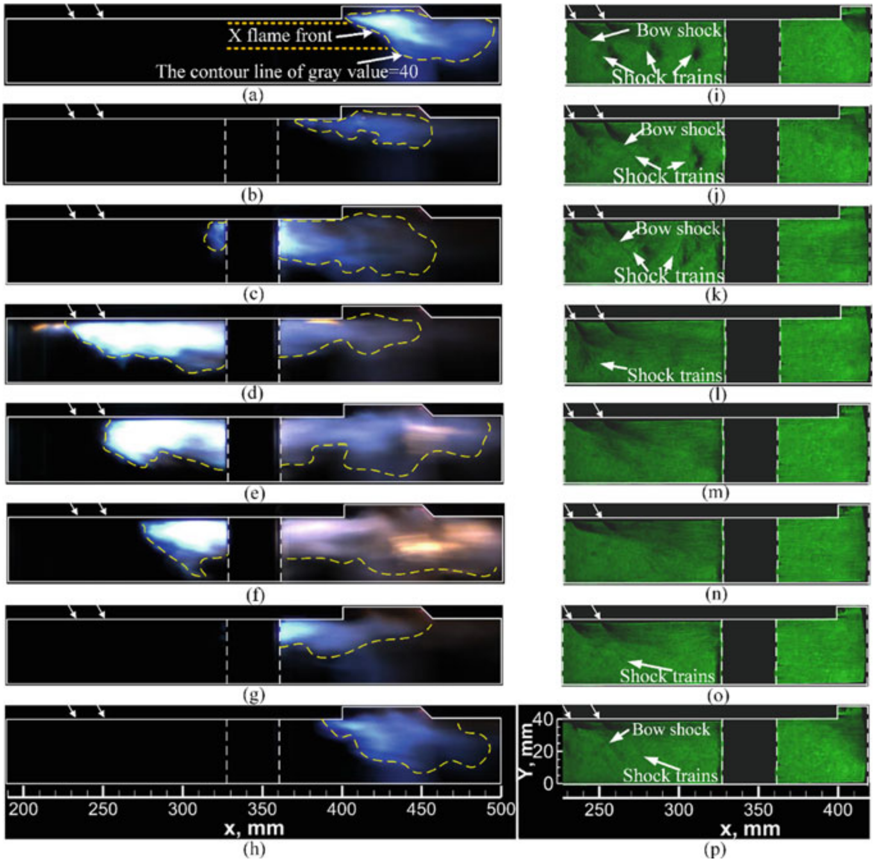

Fig. 5.17 Luminosity and schlieren visualizations of combustion oscillation for medium equivalence-ratio. The time interval between two consecutive images is 0.4 ms [21]

combustion oscillation period. Hence, a closed-loop of the flame stabilized mode is completed over one typical oscillation period.

Actually, the periodic oscillation period is a mutual transformation of scramjet and ram mode which is the same standpoint of Fotia and Driscoll [8]. Along with more combustion heat-release going into heating the air flow, the shock trains are pushed to propagate upstream as the flame propagates upstream and disappeared from the quartz windows. The combustor mode is changed from the scram mode to ram mode. Eventually, the shock trains are visualized again accompanying with the combustor mode changing from the ram to scram.

As Fig. 5.18 shows, the jet penetration is deeper because of the higher injection pressure. The higher equivalence ratio promotes more intense combustion leading to flame flashback to upstream of injector even to isolator, which can be proved by wall pressure distribution in Fig. 5.15. As schlieren images show, the shock trains cannot be visualized through the quartz windows, which is accompanied by the weak bow shock. It indicates that the flow has transitioned from a confined supersonic core flow to a pseudo shock accompanied subsonic flow, thus, combustor mode changing from the scram to ram.

The flame structures of the cases from 4 to 6 are analogous to case 2 and can also flashback to injectors. Hence, it only gives initial schlieren image in rest of the subsections for purpose of avoiding repetition.

In order to quantitatively investigate the experimental flame oscillation characteristics, Following the method of Micka [23], 42,000 total images were analyzed for 7 cases to characterize the combustion zone outline by iso-luminosity contours of gray value = 40. The averaged streamwise locations of the flame front are then calculated in range of y = 20–40 mm. The flame propagation speed can be obtained by the flame front positions and the corresponding time intervals. The probability density of flame propagation speed can be obtained by statistics of a number of discrete flame propagation speeds within the certain width interval of 50 m/s. The power spectrum of flame front oscillation frequency obtains by Fast Fourier Transform (FFT). Although the existence of error caused by the discontinuity and limitation of the quartz windows, the general trend should not change qualitatively.

Figure 5.19 is the global view of time history of flame front position. For the convenience of analyzing, only zoom views are given below. Some interesting trends are observed. For case 1 (as seen in Fig. 5.20), since there is only a stable combustion downstream of the cavity, the flame front is maintained at the rear of the cavity and the cavity shear layer. The propagation speed relative to the combustor (see Fig. 5.21) is concentrated within the 100 m/s region corresponding with the small spatial movements of the flame front. For cases 2 and 3, the increasing proportion of flame front surrounding the injector demonstrates that the flame can be held around

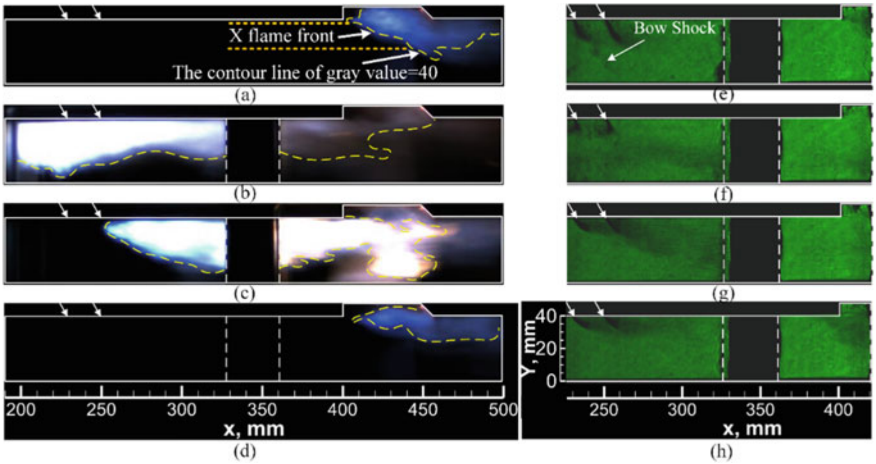

Fig. 5.18 Luminosity and schlieren visualizations of combustion oscillation for high equivalence-ratio. The time interval between two consecutive images is 1 ms [21]

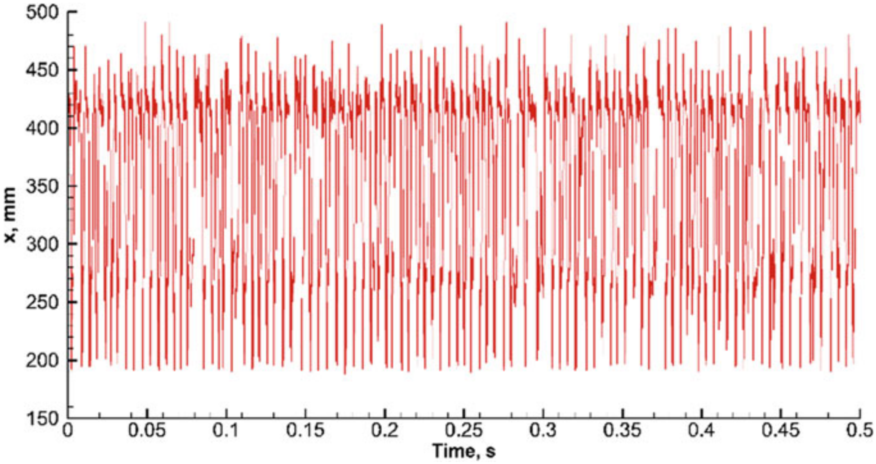

Fig. 5.19 Global view of time history of flame front position [21]

Fig. 5.20 Time history of flame front position in cases 1–3 [21]

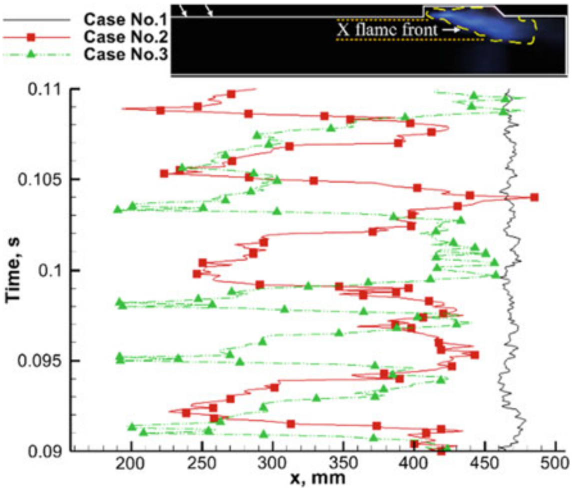

the injector easily. The main values of propagation speed focus on the range between −400 and 400 m/s. Although the speed histogram of cases 2 and 3 is similar, case 3 has slightly higher probability in range of −100 to 100 m/s. The same conclusion can be found in the propagation speed graph (Fig. 5.22), in which the distinct dominant frequency of case 3 is higher than case 2.

The effect of pre-mixing distance

In this part, effects of the different fuel mixing distances on combustion oscillation are investigated (Table 5.8). From schlieren visualizations (see Fig. 5.23), the position and structure of the bow shocks in the two cases exhibit huge differences

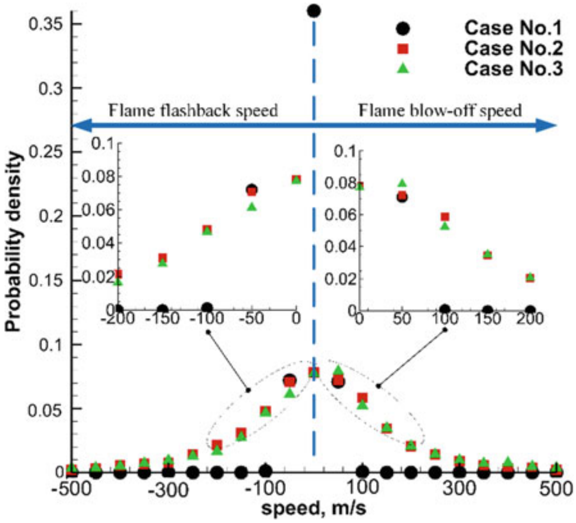

Fig. 5.21 Probability density of flame propagation speed in cases 1–3 [21]

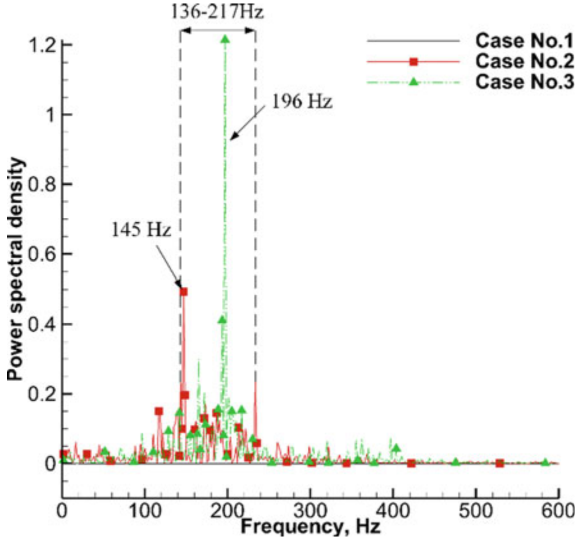

Fig. 5.22 Power spectral density of flame front oscillation in cases 1–3 [21]

Table 5.8 Comparative experiments of the influence of pre-mixing distance

Case	Total injection pressure/fuel-equivalence ratio	f_1 and f_2 injector	Outcome
4	$P_{jet} = 2.1$ MPa/$\Phi = 0.28$	$\varphi = 90°$	Periodic oscillation
5	$P_{jet} = 2.1$ MPa/$\Phi = 0.28$	$\varphi = 90°$ $L_2 = 110$ mm	Periodic oscillation

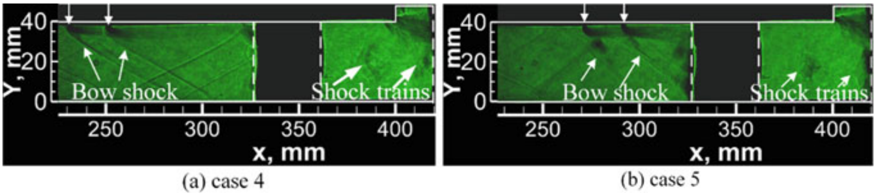

(a) case 4

(b) case 5

Fig. 5.23 Schlieren visualizations of combustion oscillation in cases 4 and 5 [21]

Fig. 5.24 Time history of flame front position in cases 4 and 5 [21]

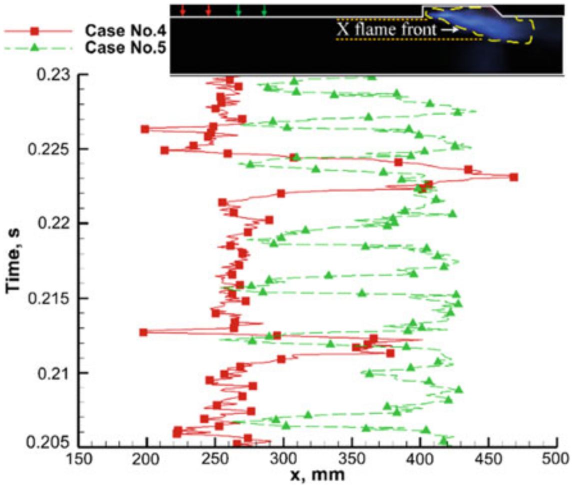

because of the different premixing distances. From the second quartz window, the pre-combustion shock trains exist in the upstream of cavity, which push the bow shock closer to the upstream in case 5. From Fig. 5.24, the reason for different flame front position may be explained as follows. Owing to longer premixing distance in case 4, the more effective fuel-mixing promotes the combustion which holds the flame around the injector for sufficiently long time. Hence, the flame propagation speed in case 4 is lower than case 5 (Fig. 5.25). The corresponding distinct dominant frequency can be obtained, which are about 64 and 335 Hz (see Fig. 5.26).

The effect of injection degree

In the present section, Table 5.9, Figs. 5.27, 5.28, 5.29 and 5.30 compare the effect of injection degree. As explained by Ref. [24], the recirculation upstream of the injectors is caused by the suction of injection. Comparing the schlieren images carefully, it can been find that increasing the injection angle leads to a stronger bow shock and a bigger separation region. The sharper injection angle promotes the larger recirculation region, and more injection mess enter the thick the boundary layer, resulting in higher fuel mixing. The recirculation region plays a vital role on mixing and consequently cases 4, 5, and 6 show better mixing performance. Under this effect, the combustion intensity in the cavity and separated boundary layer downstream of the

Fig. 5.25 Probability density of flame propagation speed in cases 4 and 5 [21]

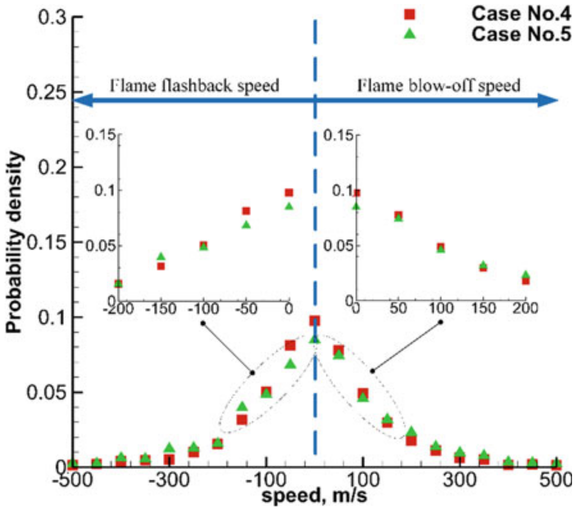

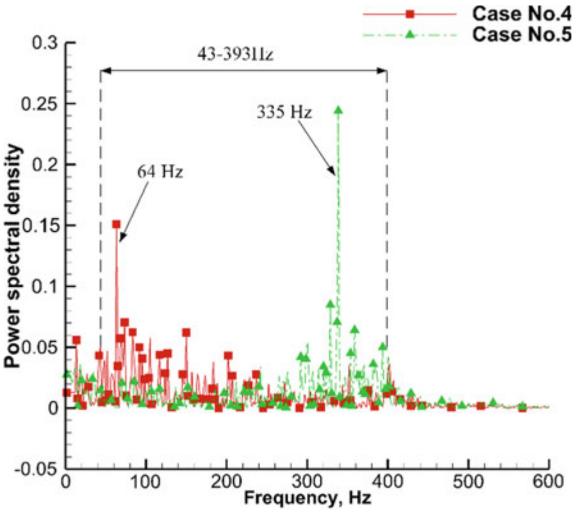

Fig. 5.26 Power spectral density of flame front oscillation in cases 4 and 5 [21]

cavity is gradually enhanced, forcing the pre-combustion shock trains and the bow shock to move forward. Under the interaction between combustion and separation region, the flame occupies the flow channel and forms a thermal throat, thus triggering flame flashback. It is worth emphasizing that case 6 not only generates the stronger bow shock, but also the compression to the bulk flow, where the fluctuation frequency and flame propagation speed are lower.

Table 5.9 Comparative experiments of the influence of injection degree

Group	Case	Total injection pressure/fuel-equivalence ratio	f_1 and f_2 injector	Outcome
1	1	$P_{jet} = 2.1$ MPa/$\Phi = 0.28$	$\varphi = 60°$	Stable combustion
	4	$P_{jet} = 2.1$ MPa/$\Phi = 0.28$	$\varphi = 90°$	Periodic oscillation
2	5	$P_{jet} = 2.1$ MPa/$\Phi = 0.28$	$\varphi = 90°$ $L_2 = 110$ mm	Periodic oscillation
	6	$P_{jet} = 2.1$ MPa/$\Phi = 0.28$	$\varphi = 120°$ $L_2 = 110$ mm	Periodic oscillation

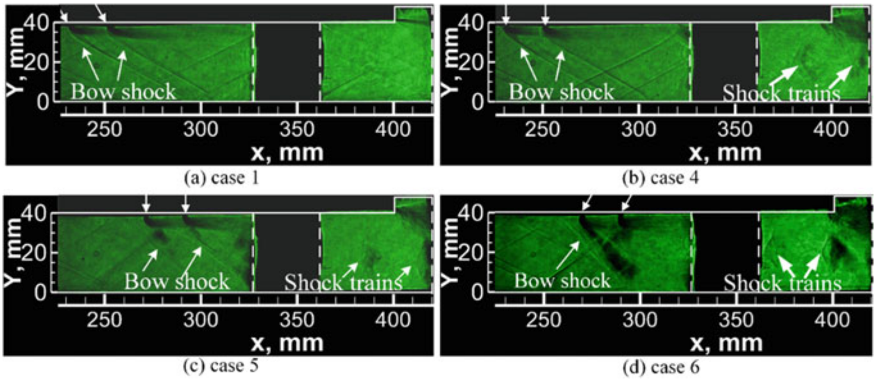

(a) case 1 (b) case 4

(c) case 5 (d) case 6

Fig. 5.27 Schlieren visualizations of combustion oscillation in cases 1, 4, 5, and 6

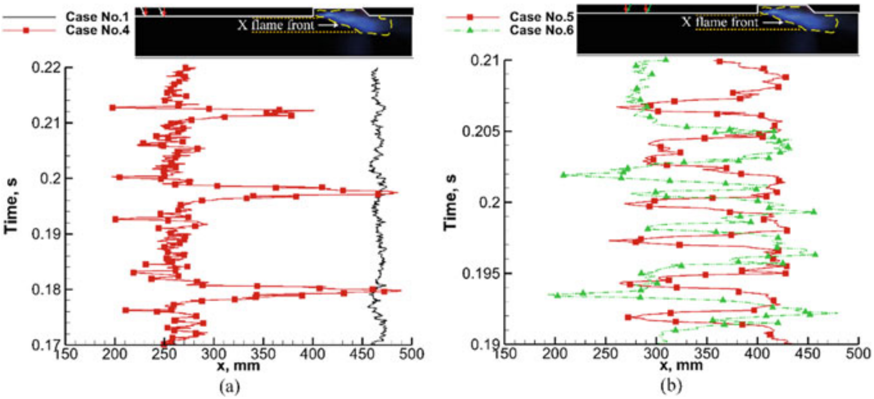

(a) (b)

Fig. 5.28 Time history of flame front position in cases 1, 4, 5, and 6 [21]

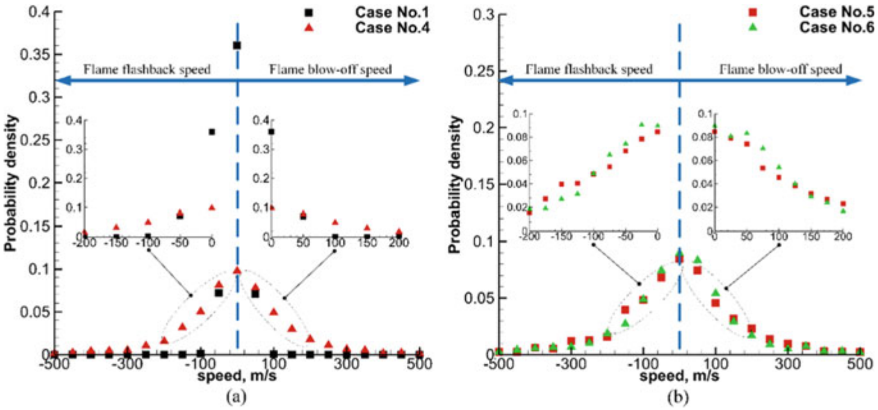

Fig. 5.29 Probability density of flame propagation speed in cases 1, 4, 5, and 6 [21]

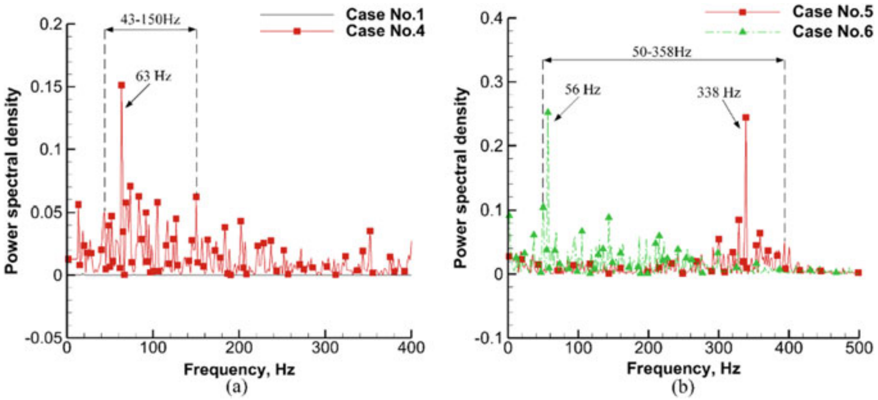

Fig. 5.30 Power spectral density of flame front oscillation in cases 1, 4, 5, and 6 [21]

The effect of jets number

In the present section, Table 5.10, Figs. 5.31, 5.32, 5.33 and 5.34 compare the effect of jets number. Compared with case 1, despite the higher fuel-equivalence ratio, the single-jet case only promotes the lower jet penetration depth, where the weaker bow shock exists. According to Pudsey and Boyce [25], the multi-jets act to enhance the near field mixing, thus improving overall mixing efficiency when compared with the dual-jet case. Compared with case 3, although the longer premix distance, case 7 only exhibits the stable combustion anchored in cavity layer, without interacting with boundary-layer. The weaker combustion could not generate pre-combustion shock trains in flow field.

Table 5.10 Comparative experiments of the influence of jets number

Case	Total injection pressure/fuel-equivalence ratio	f_1 and f_2 injector	Outcome
3	$P_{jet} = 2.7$ MPa/$\Phi = 0.37$	$\varphi = 60°$	Periodic oscillation with inlet unstart
7	$P_{jet} = 2.7$ MPa/$\Phi = 0.37$	Dual-jet $\varphi = 60°$ $L_2 = 170$ mm	Stable combustion

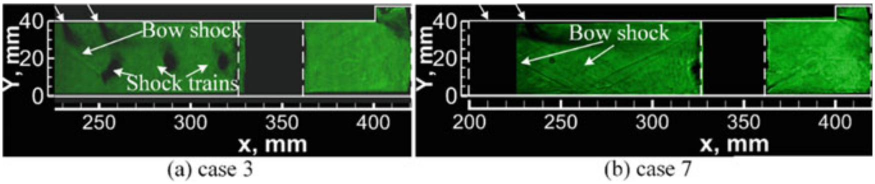

Fig. 5.31 Schlieren visualizations of combustion oscillation in cases 3 and 7 [21]

Fig. 5.32 Time history of flame front position in cases 3 and 7 [21]

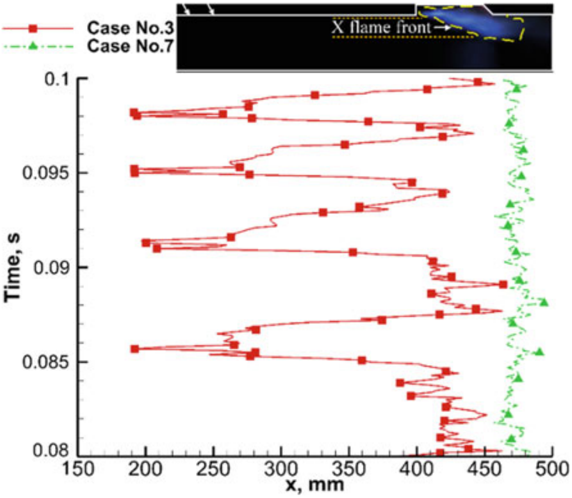

5.2.1.3 Effect of Cavity Parameters

The detailed flow conditions and outcomes are listed in Table 5.11. Three groups of comparative cases respectively investigate the effects of cavity length-to-depth ratio, aft ramp angle of the cavity, and air throttling distance downstream of the cavity on combustion oscillation phenomenon.

In Fig. 5.35 there is no combustion oscillation for case 1, only the stable combustion is maintained downstream of the cavity. An expansion wave (as indicated in the schlieren photograph by its light colour) is observed at the separation corner of

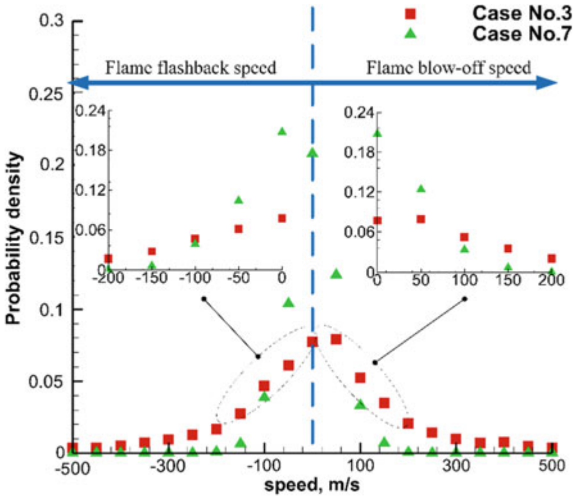

Fig. 5.33 Probability density of flame propagation speed in cases 3 and 7 [21]

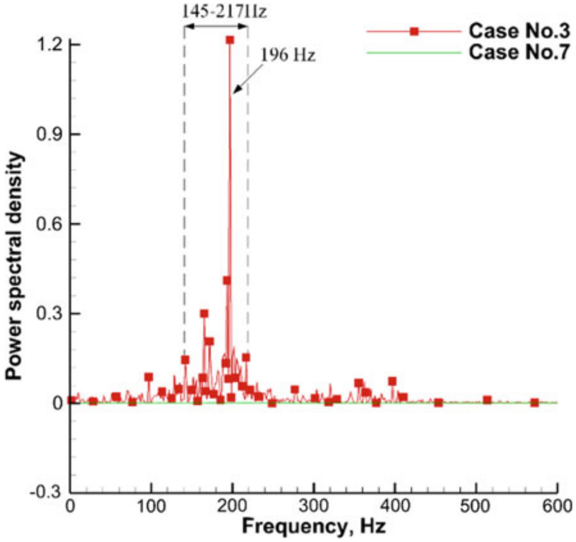

Fig. 5.34 Power spectral density of flame front oscillation in cases 3 and 7 [21]

leading edge of the cavity. In addition, the injection bow shock and its reflect shock exist all the time, which indicates the flow field maintains supersonic. From the separation of the boundary layer at the leading edge of the cavity, a shear layer is formed, which extends toward the cavity floor. The separated boundary layer upstream of the cavity is too thin to hold flames. Hence, the flames are stable in cavity shear layer. Note that the core flow direction in all photographs is from left to right. The shadow between the two quartz windows is the combustor supporting structure. Due to the limitation of experimental equipment, schlieren image only shows the region

Table 5.11 The cavity parameters of comparative cases

Group	Case	Total injection pressure/fuel-equivalence ratio	Cavity aft ramp angle/cavity length/N_2 injector distance	Outcome
1	1	$P_{jet} = 2.4$ MPa/$\phi = 0.34$	$L = 40$ mm	Stable combustion
	2	$P_{jet} = 2.4$ MPa/$\phi = 0.34$	$L = 56$ mm	Periodic oscillation
2	3	$P_{jet} = 2.1$ MPa/$\phi = 0.28$	$\theta = 45°$	Stable combustion
	4	$P_{jet} = 2.1$ MPa/$\phi = 0.28$	$\theta = 90°$	Periodic oscillation
3	5	$P_{jet} = 2.1$ MPa/$\phi = 0.28$	$P_{N2} = 0.5$ MPa/$L_4 = 30$ mm	Stable combustion
	6	$P_{jet} = 2.1$ MPa/$\phi = 0.28$	$P_{N2} = 0.5$ MPa/$L_3 = 10$ mm	Periodic oscillation

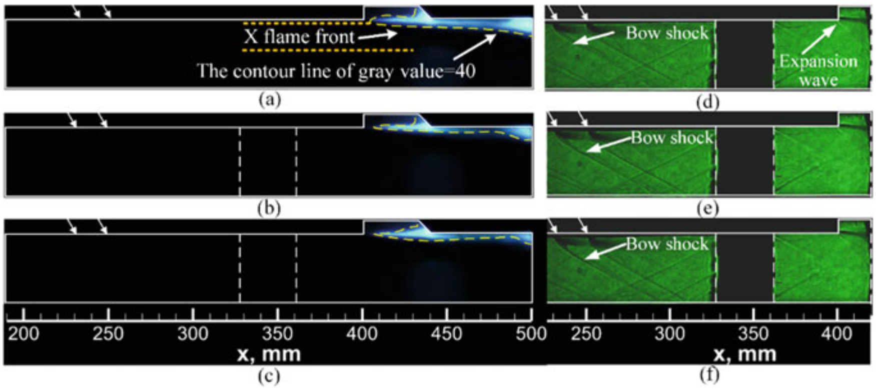

Fig. 5.35 Luminosity and schlieren visualizations of stable combustion for case 1. The time interval between two consecutive images is 2 ms [27]

between fuel injectors and leading edge of cavity. The flame frames of case 3 and case 5 are analogous to case 1, so they have been omitted to avoid repetition.

Figure 5.36 shows the large-amplitude combustion oscillation which can be divided into three distinctive stages such as flame flashback (Fig. 5.36a–c, i–k, q–s), flame blown off (Fig. 5.36d–g, l–o, t–w) and flame re-holding (Fig. 5.36h, p, x). At the beginning, the flames are maintained in the cavity and downstream of the cavity. For some reasons (which will be detailed investigated in following subsections), the intense combustion occurs in the cavity and boundary layer downstream of the

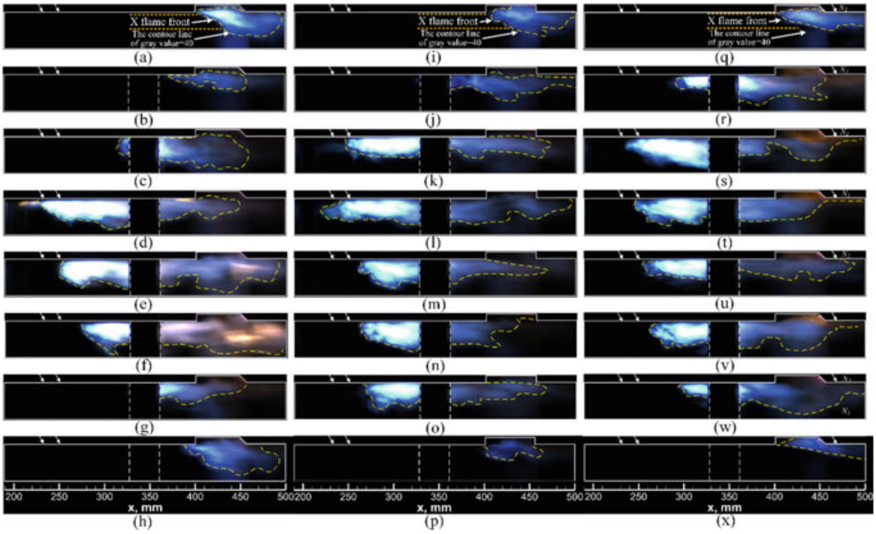

Fig. 5.36 Luminosity visualizations of combustion oscillation for cases 2, 4 and 6 (Each column). The time intervals between two consecutive images for each case are 0.4, 0.5 and 1 ms [26]

cavity. By accumulating the energy from the exothermic reactions, the combustion intensity in the separated boundary layer is gradually enhanced. The flames occupy the flow channel forming a thermal throat. Then, the flames begin to propagate from the leading edge of the cavity wall to the fuel injectors. The flame core rapidly moves upstream along the combustor wall, until reaches the fuel injectors location.

As schlieren images at the flame flashback stage (Fig. 5.37a–c, i–k, q–s) show, pre-combustion shock trains near the fuel injector are gradually pushed forward, and jet penetration depth are increased. During the flame flashback process, as we know, the shock waves confine a high-pressure, high-temperature, low-speed region. The increased fuel residence time promotes fuel mixing, leading to enhanced combustion intensity downstream of the cavity. The increased heat release rate leads to separated boundary layer enlarged. So far, the thermal throat is formed and forces the flames propagate upstream. After the flame flashback stage, due to the lack of the fuel premixing effect, the local equivalence ratio is lost. Hence, the flames surrounding the injector cannot be sustained, and they are blown quickly back to the cavity. The flames then are re-stabilized in the rear of the cavity and the cavity shear layer, forming the cavity stabilized mode flames again. According to the corresponding schlieren images (Fig. 5.37l–o, t–w), the core flows are supersonic during flame blown off stage. In contrast, Fig. 5.37d–g show a subsonic flow. At this stage, the separation zone is pushed downstream owing to lack of heat release blockage. At the flame re-holding stage, the flames are held in the cavity shear layer again, preparing for triggering of the next combustion oscillation period. Hence, a closed-loop of the flame stabilized mode is completed over one typical oscillation period. It can be concluded that, the boundary layer separation is the necessary condition of the

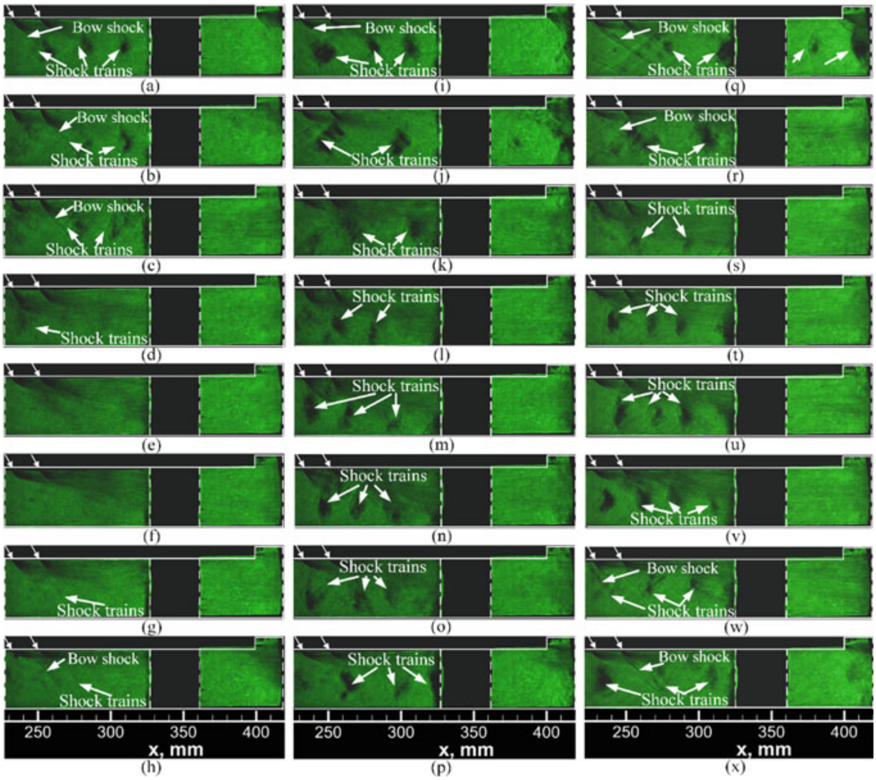

Fig. 5.37 Schlieren visualizations of combustion oscillation for cases 2, 4 and 6 (Each column). The time intervals between two consecutive images for each case are 0.4, 0.5 and 1 ms [26]

flashback, and it will result in thermal throat which plays a crucial role in the stability of combustion and in triggering flame flashback.

In order to quantitatively investigate the experimental combustion oscillation characteristics, following the method of Micka [23], 36,000 total images are analyzed for 6 runs to characterize the combustion zone outline by iso-luminosity contours of gray value = 40. The average streamwise location of the flame front is then calculated for y = 20–40 mm. In the following analysis, figures show the streamwise position of the flame front (Fig. 5.38) the streamwise propagation speed of the flame front calculated by flame front position and corresponding time interval (Fig. 5.39) and power spectrum of flame front oscillation frequency obtained by Fast Fourier Transform (FFT) (Fig. 5.40). Although the existence of error caused by the discontinuity and limitation of the quartz windows, the general trend should not change qualitatively.

For cases 1, 3 and 5, since there are only stable combustions downstream of the cavity, the flame fronts are maintained at the rear of the cavity. The propagation speeds relative to the combustor are concentrated within the 100 m/s region corresponding with the small spatial movements of the flame front. The corresponding dominant

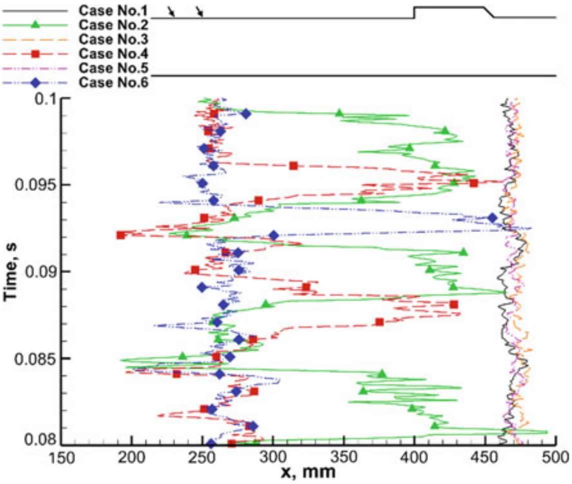

Fig. 5.38 Time history of flame front position in different cases [26]

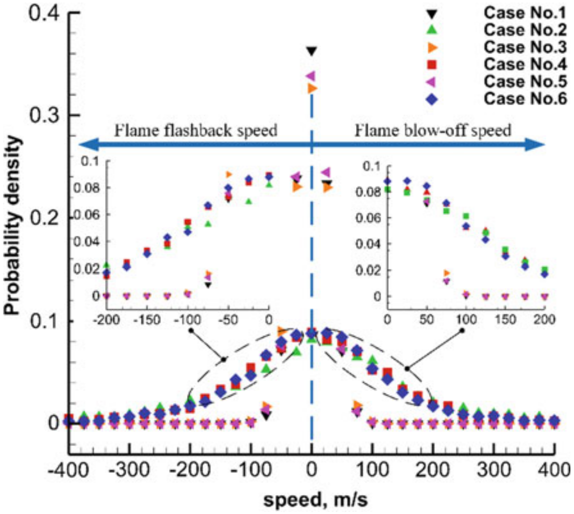

Fig. 5.39 Probability density of flame propagation speed in different cases [26]

frequency cannot be distinguished. For cases 2, 4 and 6, the increasing proportion of flame front surrounding the injector demonstrates that the flames can be held around the injector easily. The combustion oscillation frequency appears as the opposite trend compared with flame front. However, the flame speeds in these cases are similar, both flame flashback and flame blow-off speeds are stable within 300 m/s relative to the combustion chamber.

Figure 5.41 shows the average pressure distribution along the model combustor upper wall. For all cases, the isolator keeps the flow steady, and pressure fluctuations only start at the fifth measurement point. In cases 1, 3 and 5, stable combustions are mainly concentrated in the cavity and the boundary layer downstream of the

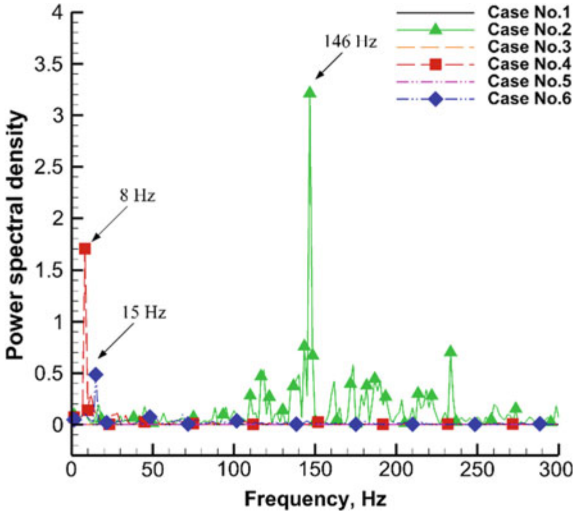

Fig. 5.40 Frequencies spectral density of flame front oscillation in different cases [26]

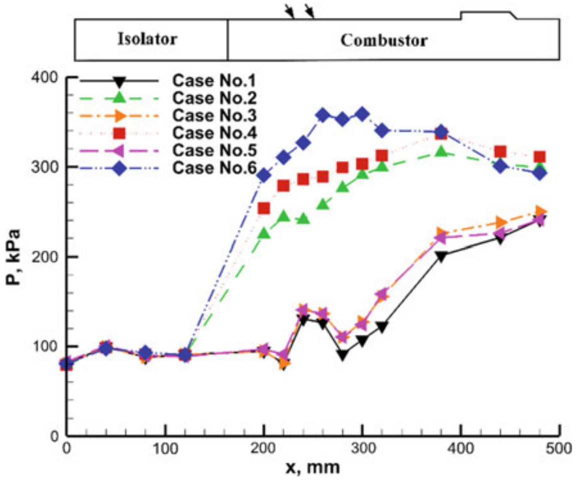

Fig. 5.41 Wall pressure distribution for different cases along the upper wall [26]

cavity, with a peak pressure of about 240 kPa. In contrast, as will be discussed in following section, the larger length-to-depth ratio, stronger cavity aft ramp angle and closer air throttling downstream of the cavity induce flame flashback. The increasing proportion of flame front sustaining near injectors causes the pressure increase near injectors, whose corresponding peak pressure is about 350 kPa, whereas the pressure in cavity and downstream of it is a little bit lower.

The effect of cavity length-to-depth ratio

In this subsection, the effects of the different cavity length-to-depth ratio on combustion oscillation are investigated as the first group. For case 1, although the total injection pressure improves to 2.4 MPa ($\phi = 0.34$), there is no combustion oscillation, only a stable combustion is maintained in cavity shear layer and downstream of the cavity. However, the combustion oscillation accompanying with rapid flame flashback occurs in case 2. As reference analysed [18, 27], We suppose that cavity length will act on the combustion oscillation mainly through the recirculation volume in the cavity and the mass and heat exchange between cavity shear layer and the core flow. With $L = 40$ mm in cavity, the shorter length limits the hear release in the cavity and mass and heat exchange which leads to a stable flame anchored at the cavity. As Luminosity and schlieren images show, the longer cavity length promotes the heat release and the mass and heat exchange between cavity shear layer and the core flow. Compared with case 3, the higher injection pressure leads to the higher global equivalence ratio further the more intense combustion. All above factors will generate intense combustion in cavity and downstream of the cavity, where the flame interacts with boundary layer and gradually occupies the flow channel further forming a thermal throat to trigger flame flashback phenomenon. At flame flashback and flame blown off stages, as schlieren images show, pre-combustion shock trains near the fuel injector are gradually pushed forward, disappear and re-appear upstream. The flame front in case 2 can flashback from cavity to injector, however it cannot be sustained surrounding the injector, and is blown off quickly back to the cavity. Hence, the proportion of flame front surrounding the injector in case 2 is lower than other flame flashback cases. The corresponding dominant frequency is higher than other cases.

The effect of cavity aft ramp angle

In this subsection, the effects of aft ramp angle are studied by the comparative experiments listed in group 2. Compared with case 3, the sharper cavity aft ramp angle in case 4 leads to combustion oscillation. We suppose that cavity aft ramp will act on the combustion oscillation mainly through the impinging shock wave in the cavity aft ramp and the mass and heat exchange between cavity shear layer and the core flow. When the angle turns from 45° to 90°, however, it will maybe result in significant strong impinging shock wave. As Zare-Behtash et al. [28] analyze, the impinging shock occurs over the cavity and on the shear layer, however the interaction results in a similar interaction as with the boundary layer [29], namely the lifting of the shear layer. On the other hand, with sharper cavity aft ramp, a region of reversed flow near shear layer is sometimes created. The roll-up and fall-off derived from the velocity deviation between cavity shear layer and the core flow promote the mass and heat exchange between cavity shear layer and the core flow. From Fig. 5.38, the increasing proportion of flame front surrounding the injector demonstrates that the flames can be held around the injector easily. The same conclusion can be found in the propagation speed spectra (Fig. 5.40).

The effect of air throttling downstream of the cavity

Group 3 investigates the effects of the air throttling locations downstream of the cavity on combustion oscillation. As reference analysed [30], air throttling can enlarge wall boundary and decrease the flow velocity. For case 5, owing to air throttling far away from downstream of the cavity, the separated boundary layer doesn't significantly interact with combustion. There is no thermal throat to introduce flame flashback phenomenon. Hence, only stable flames anchor at the cavity. For case 6, the closer air throttling is loaded near downstream of the cavity. The improved fuel/air mixing in the separated boundary layer leads to the combustion intensity in the cavity and separated boundary layer downstream of the cavity gradually enhanced. The flames occupy the flow channel and form a thermal throat thus triggering flame flashback. It is worth stressing that, by means of air throttling, the boundary layer separation in case 6 is easier and can sustain longer. Hence, case 6 has more proportion of flame front surrounding the injector and lower fluctuation frequency.

5.2.2 Numerical Investigations of Flame Flashback

5.2.2.1 Numerical Condition

In the present study, the fifth-order weighted essentially non-oscillatory scheme developed by Jiang and Shu [31] is used for inviscid fluxes and the second-order centre scheme is used for viscous fluxes. To improve the computational efficiency, time integration is performed using a second-order implicit dual-time-step approach [32], the inner iteration of which is achieved through a lower upper symmetric Gauss-Seidel method. The acoustic CFL number is 0.5.

Geometry and boundary conditions
A sketch of the computational domain is shown in Fig. 5.42. The isolator is set to 200 mm long for better turbulent boundary. For purpose of reducing computational burden, the computational domain has a constant width of 10 mm. For illustrative purpose of effect of wall boundary condition on flame flashback mechanism, a no-slip, no-penetration adiabatic condition or symmetry boundary condition which does not impose boundary layer is set at upper wall, a periodic condition is used on both sides and a no-slip, no-penetration adiabatic condition is imposed at all lower walls. The fuel is injected sonically from two 1-mm-diameter injectors located 110

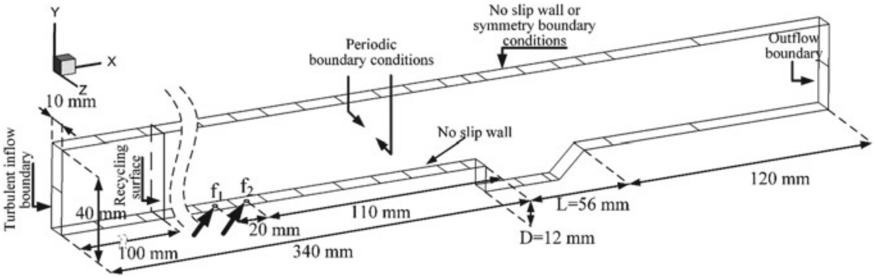

Fig. 5.42 Schematic diagram of the computation domain and boundary conditions [33]

and 130 mm upstream of the cavity leading edge. A turbulent boundary-layer with $\delta_{inf} = 3$ mm is adopted for the present study. This thickness is estimated based on an advanced two-dimensional RANS simulation.

The entire domain is divided into 44 blocks for parallel computing, consisting of 40 blocks in the main flow and 4 blocks in the cavity.

Turbulence models

The governing equations have been well described in the previous literatures [34] and omitted here for brevity. A hybrid LES/RANS method [35] is adopted. This method combines the Spalart-Allmaras (S-A) RANS model [36] which is used for near-wall regions and the Yoshizawa sub-grid scale model [37] which is used for regions away from the wall. While the interaction between the turbulence and chemistry is neglected in the RANS region. The basic assumption in the present hybrid method is that the RANS region is considerably thin (~$0.1\delta_{\mathrm{inf}}$, where δ_{inf} is the inflow thickness). Therefore, only a significantly small portion of the combustion may occur in the RANS region. Neglecting the interaction between the turbulence and chemistry in this region is believed to negligibly influence the results. An assumed sub-grid PDF (Probability Density Function) closure model [38] is used for turbulence-chemistry interaction.

A recycling/rescaling method is used to treat the turbulent inflow condition, which is considered to be a promising way to prescribe time-dependent turbulent inflow conditions for LES or hybrid RANS/LES of spatially developing turbulent flows [39–42]. In the present study, a method similar to that of Xiao et al. [41] is used.

5.2.2.2 Effects of Chemical Kinetic Mechanism

To reduce computation costs and identify the most important chemical paths, the reduced chemical kinetic mechanism of seven species and three steps for ethylene/air combustion [43] (denotes as Original Mechanism) is used and outlined in Table 5.12. Note that accurate prediction of the reaction process and flame temperature is not expected. Nonetheless, at the very least, reasonable macro-effects of heat release on combustion should be obtained.

Figure 5.43 presents the ignition delay time of ethylene/air mixtures obtained using CHEMKIN 4.1 with the reduced chemical kinetic mechanism [44]. This figure

Table 5.12 Reduced chemical kinetic mechanism of seven species and three steps for ethylene/air combustion

Reaction	A (cm^3/mol s)	b	T_a (K)
$C_2H_4 + O_2 \Leftrightarrow 2CO + 2H_2$	2.100E+14	0.0	18015.3
$2CO + O_2 \Leftrightarrow 2CO_2$	3.450E+11	2.0	10134.9
$2H_2 + O_2 \Leftrightarrow 2H_2O$	3.000E+20	−1.0	0.00

Fig. 5.43 Comparison of experimental ignition delay data with calculated data using different reaction mechanism and calculated ignition delays with the $C_2H_4/O_2/Ar$ mixture at $\varphi = 1$, Ar = 96% , P ≈ 3 atm

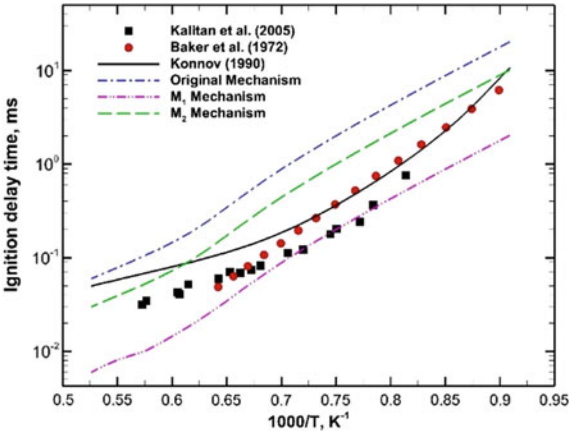

compares the calculated ignition delays of the C2H4/O2/Ar mixture with experimental data reported by Kalitan et al. [45], Baker et al. [46], and Konnov [47], validating the reduced chemical kinetic mechanism. The maximum of pressure gradient is used as the ignition criterion in accordance with the experimental counterpoint. Within a range of 1100–1900 K, the ignition delay time is overestimated or underestimated using the original and the first modified ethylene/air chemical kinetic mechanism (denotes as M1 Mechanism in which the pre-exponential factor is modified as $A_1^* = 10 \times A$, where A stands for pre-exponential factor of Original mechanism), respectively. Hence, a considerable longer or shorter time is required to reach the reaction temperature. In particular, when the temperature decreases, the ignition delay time shows a big difference from the experimental value. The ignition delay time for the second modified ethylene/air chemical kinetic mechanism (denotes as M2 Mechanism in which the pre-exponential factor is modified as $A_2^* = 2 \times A$) remains different from the experimental value; nonetheless, the difference is significantly reduced. Thus, the M2 ethylene/air chemical kinetic mechanism is adopted in the following sections.

5.2.2.3 Effects of Boundary-Layer Conditions

In this section, the boundary-layer effect on flame flashback will be investigated. The boundary, disturbance and flame flashback status are listed in Table 5.13.

Based on the above analysis, it is apparent that the cavity is a key component for promotion of stable combustion. In addition, different boundary conditions affect the flame flashback phenomenon in the combustor with the cavity flameholder. As is apparent from Fig. 5.44, the result of case 1 exhibits a strong flame flashback phenomenon. Owing to the increasing boundary-layer effects, the large separated boundary-layer on the upper wall enhances the main flow compression. The flame mainly develops from the boundary-layer downstream of the cavity. During the flame flashback process, owing to the interaction of the separated boundary-layer and the

Table 5.13 Concise descriptions of two cases

Case	Up wall	Down wall	Disturbance condition	Outcome
No. 1	Turbulent boundary[a]	Turbulent boundary[a]	No disturbance	Flame flashback
No. 2	Symmetric boundary	Turbulent boundary[a]	No disturbance	No flame flashback

[a] Turbulent boundary-layer with 3-mm thickness

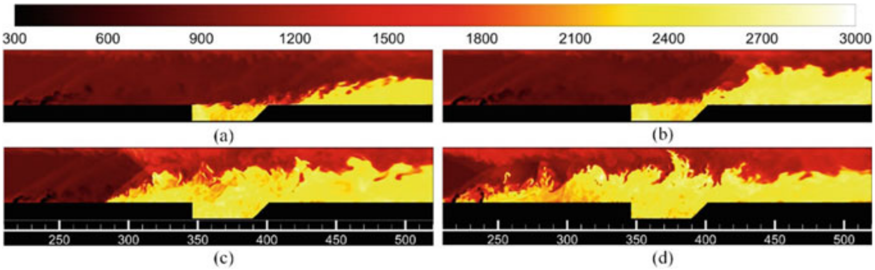

Fig. 5.44 Instantaneous temperature distribution for case 1 (The non-dimensional time interval between two images is $\Delta t = 60 \times D/U_{\infty}$; unit K) [33]

flame, the combustion intensity downstream of the cavity increases. By accumulating the energy from the exothermal reactions, the flame is gradually enhanced, further occupying the flow channel. When the energy exceeds a threshold level, the forming thermal throat triggers flame flashback phenomenon. When the downstream flame spreads to the cavity, the flame in the cavity interacts with the downstream flame and further accelerates itself, until it reaches the injection area. In contrast, there is no boundary-layer in upper wall because of the symmetric boundary condition as presented in Fig. 5.45. Hence, the compression of main flow is too weak to form a thermal choking. A stable combustion, therefore, is maintained downstream of the cavity.

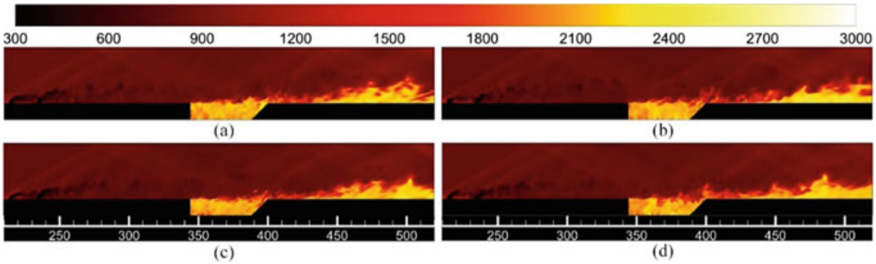

Fig. 5.45 Instantaneous temperature distribution for case 2 ($\Delta t = 60 \times D/U_{\infty}$; unit K) [33]

Although it is known that the boundary condition of case 1 causes the flame flashback phenomenon, the detailed mechanism underlying the flame flashback phenomenon remains unclear, since both temperature and pressure in the flow field differ from those in case 2. In this section, we will clarify what the sensitive parameter is. Where the sensitive region is. Figure 5.46 shows the distributions of average pressure and temperature at different y-z slices along X-axis, it is apparent that the difference of temperature is more obvious than pressure. Figure 5.47 shows the dimensionless temperature distribution along the model combustor lower wall, which also confirms the notable temperature difference downstream of the cavity. Therefore, it can be

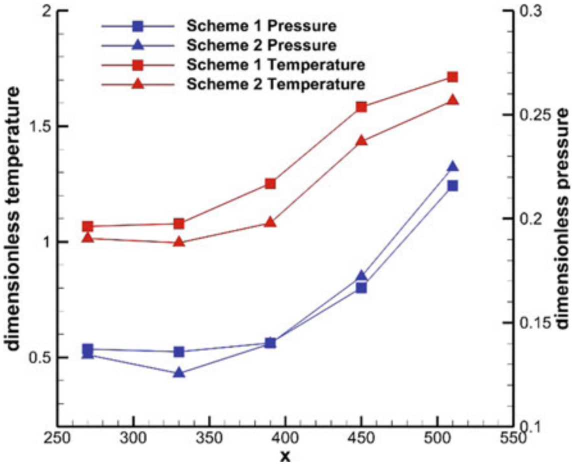

Fig. 5.46 Distributions of average dimensionless parameter along the downside wall [33]

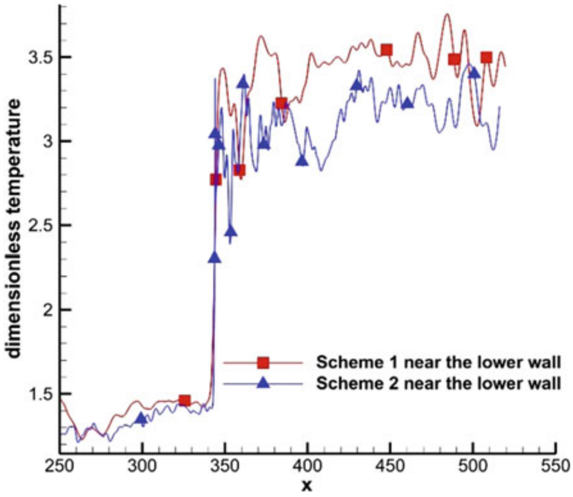

Fig. 5.47 Distributions of dimensionless temperature along downside wall [33]

concluded that the flame flashback phenomenon is sensitive to temperature fluctuation rather than pressure fluctuation, and the boundary-layer downstream of the cavity is the area sensitive to the flame flashback phenomenon.

5.2.2.4 Effects of Thermal Disturbances

Based on the above analysis, it is apparent that temperature is the sensitive parameter and the downstream region of the cavity is the sensitive area for flame flashback phenomenon. In this section, an additional thermal disturbance is loaded at downstream of the cavity to simulate the fluctuation of the local parameters. In addition, the fluctuation locations in the sensitive area should also be investigated. The boundary, disturbance and diffusion conditions, and flame flashback status are listed in Table 5.14.

Figures 5.48 and 5.49 show the instantaneous temperature distribution results for different cases. For case 3, the 30-mm-long thermal disturbance ($T = 2500$ K) is located at 72 mm downstream of the cavity, which is 12 mm upstream of the outflow boundary. For case 4, the 15-mm-long thermal disturbance ($T = 2500$ K) is located at 36 mm downstream of the cavity, which is 72 mm upstream of the outflow boundary. Although the thermal disturbance energy in case 3 is larger than case 4, the residence time of the disturbance is too short to induce the flame flashback phenomenon. This is because the thermal disturbance is close to the outflow boundary and easily blown out of the flow channel. In contrast, once the accumulated energy exceeds a certain threshold as the residence time of the disturbance increases, the small thermal

Table 5.14 Concise descriptions of three cases

Case	Up wall	Down wall	Disturbance and diffusion condition	Outcome
No. 3	Symmetric boundary	Turbulent boundary[a]	Disturbance (30 mm long) located at 72 mm downstream of cavity	No flame flashback
No. 4			Disturbance (15 mm long) located at 36 mm downstream of cavity	Flame flashback
No. 5			Increasing diffusion coefficient downstream of cavity	Flame flashback

[a] Turbulent boundary-layer with 3-mm thickness

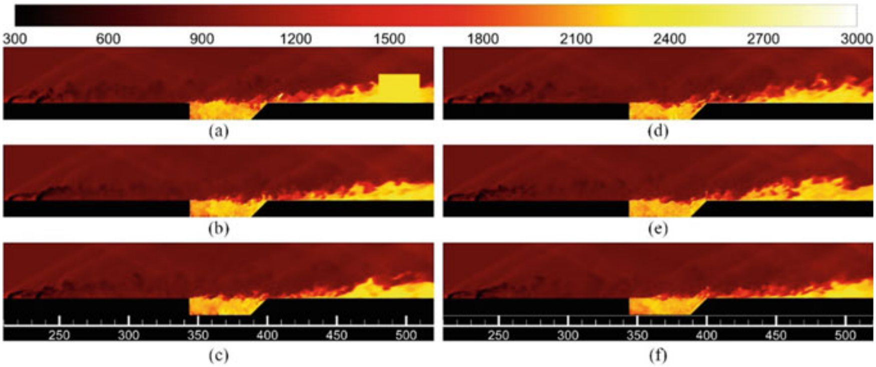

Fig. 5.48 Instantaneous temperature distribution for case 3; Disturbance (30 mm long) located at 72 mm downstream of cavity ($\Delta t = 50 \times D/U_{\infty}$; unit K) [33]

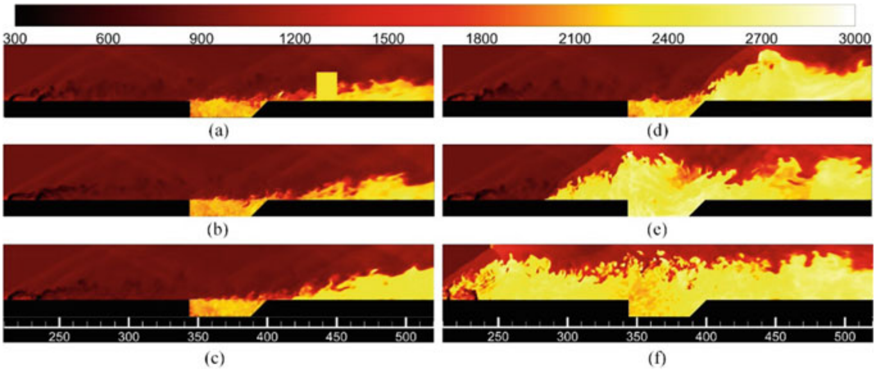

Fig. 5.49 Instantaneous temperature distribution for case 4; Disturbance (15 mm long) located at 36 mm downstream of cavity ($\Delta t = 50 \times D/U_{\infty}$; unit: K) [33]

disturbance in case 4 is amplified and spreads throughout the entire fluid flow, inducing the flame flashback phenomenon under the same incoming flow and boundary conditions. It can be demonstrated that the thermal disturbance in the sensitive area induces fluctuation of the local parameters, further enhancing the combustion. This also indicates that, with increasing residence time of the thermal disturbance, the combustion fluctuation downstream of the cavity is enhanced. Compared with the temperature distribution in case 1, although a thermal disturbance is loaded, the speed of flame flashback in case 4 is slower than case 1. As a result, when the flame front reaches the injectors location, the flame front in case 4 remains a certain distance from the injectors location.

Adjusting the diffusion coefficient of the species in the sensitive area to improve the local mixing degree is another approach to induce flame flashback. Figure 5.50 shows the temperature distribution results for case 5. The diffusion coefficient is

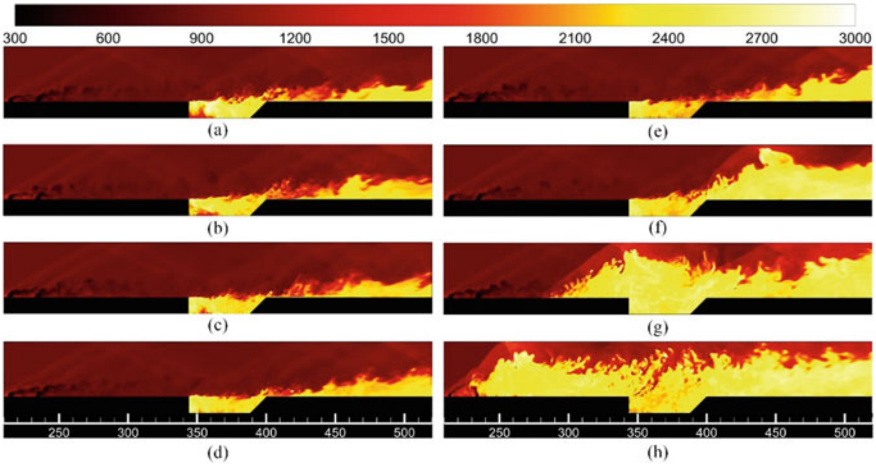

Fig. 5.50 Instantaneous temperature distribution for case 5; Increasing diffusion coefficient downstream of cavity ($\Delta t = 50 \times D/U_\infty$; unit: K) [33]

magnified to seven times bigger than original at downstream of the cavity. At the fuel and air interface, the amplified diffusion coefficient improves the mixing speed. This enhanced mixing efficiency promotes the combustion intensity. In contrast to the intense flame flashback, twice as much time is required for energy accumulation as in case 4, owing to the simply amplifying diffusion coefficient downstream of the cavity.

5.2.2.5 The Detailed Investigation of Representative Case

In the following section, detailed analyses are conducted with different methods to investigate the combustion characteristics of case 4. Figure 5.51 shows the instantaneous heat release distribution with a sonic line. Initially, the heat releases are located in the jet-with-cavity shear layer and boundary-layer downstream of the cavity, concentrating on the sonic line. During the flame flashback process, as the thickness of separated boundary-layer increasing, the heat release rate gradually increases. The heat release mainly distributes on the flame front and propagates forward from downstream of the cavity to injectors. As we can see, part of strong heat release distributes outside of the sonic line, owing to the strong interaction of turbulence and vortex. This strong heat release forms a thermal throat when the flame spreads to the cavity position and further accelerates itself, inducing flame flashback by means of interaction with a large separated boundary-layer. Under this process, the interaction between flame and separated boundary-layer gradually intensifies the combustion intensity.

Firstly, Fig. 5.52 shows the speed distribution and the coloured streamline with pressures. Figure 5.53 gives the instantaneous pressure distribution. Compared with

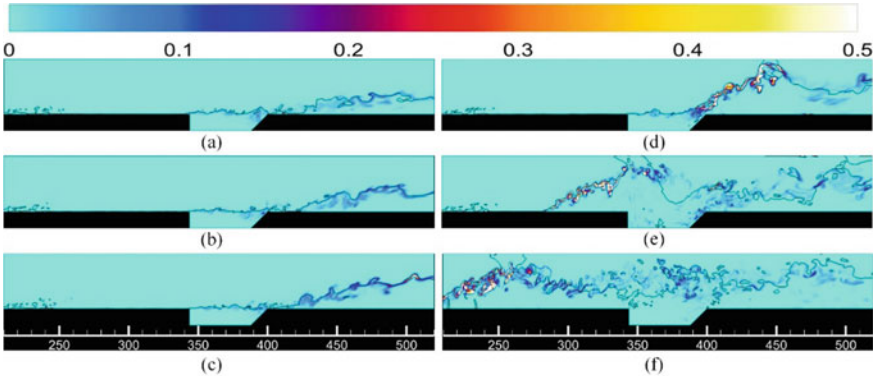

Fig. 5.51 Instantaneous heat release distribution with sonic line for case 4 ($\Delta t = 50 \times D/U_\infty$) [33]

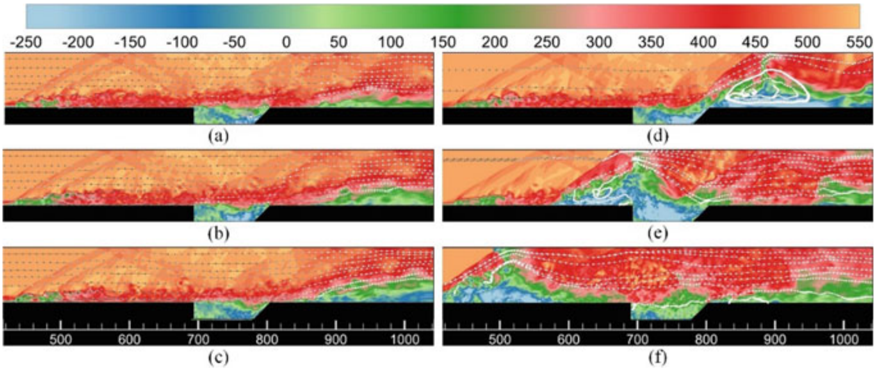

Fig. 5.52 Instantaneous speed distribution and streamline coloured with pressure for case 4 ($\Delta t = 50 \times D/U_\infty$; unit: m/s) [33]

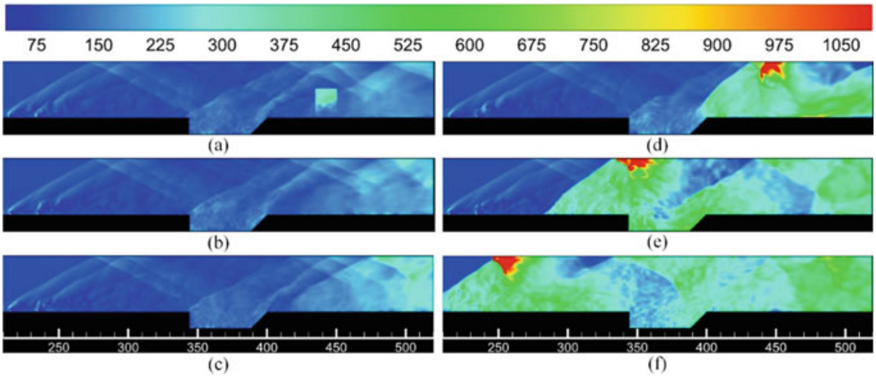

Fig. 5.53 Instantaneous pressure distribution for case 4 ($\Delta t = 50 \times D/U_\infty$; unit: KPa) [33]

Fig. 5.49, it can be found that the most of flame is located in the low speed region. During the flame flashback process, the shock wave confines a high-pressure, high-temperature, low-speed region. All these effects lead to higher combustion intensity downstream of the cavity. The back pressure generated from the heat release promotes the boundary-layer to separate. Conversely, the back pressure accompanying the separated boundary-layer gradually occupies the main flow and the forms thermal throat to trigger flame flashback.

As shown in Fig. 5.54, the high pressure appears at downstream of the cavity. Owing to the enhancement of combustion intensity, the pressure peaks which are located at the flame front at the upper and lower wall increase. During the flame flashback process, the magnitude of pressure peaks in upper and lower walls may have the same order of the fuel injection. It is indicated that, since the thermal disturbance enhances the heat release downstream of the cavity, the higher pressure causes the bulk flow to be compressed. It is apparent in Fig. 5.55 that the main distribution of the heat release concentrates on the flame front. The interaction between flame

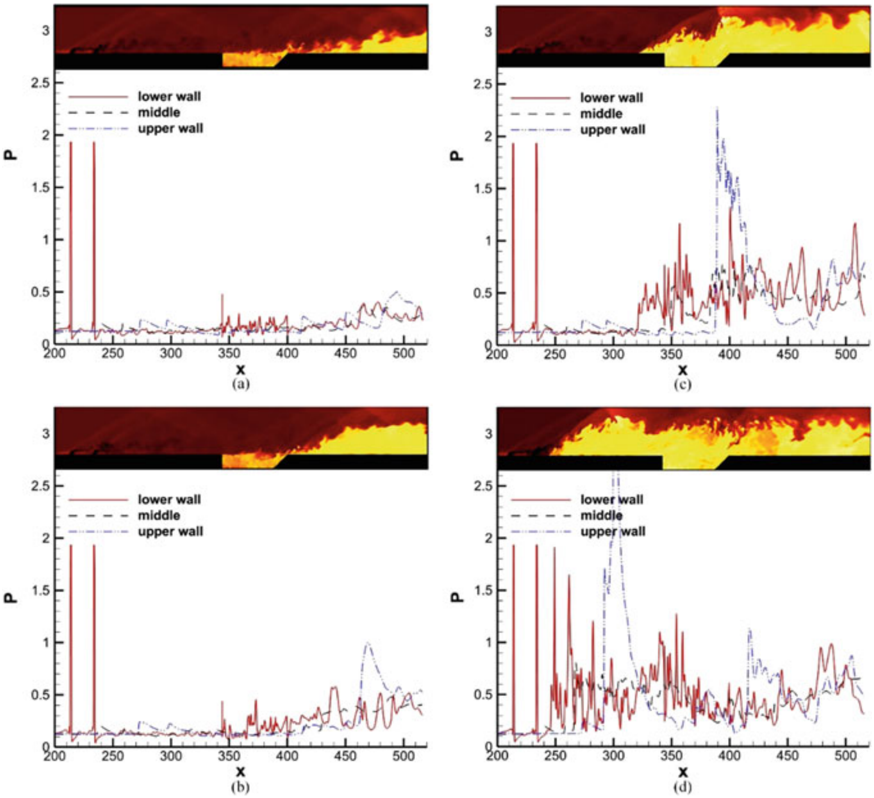

Fig. 5.54 Non-dimensional pressure distributions in three vertical positions for case 4 ($\Delta t = 50 \times D/U_{\infty}$) [33]

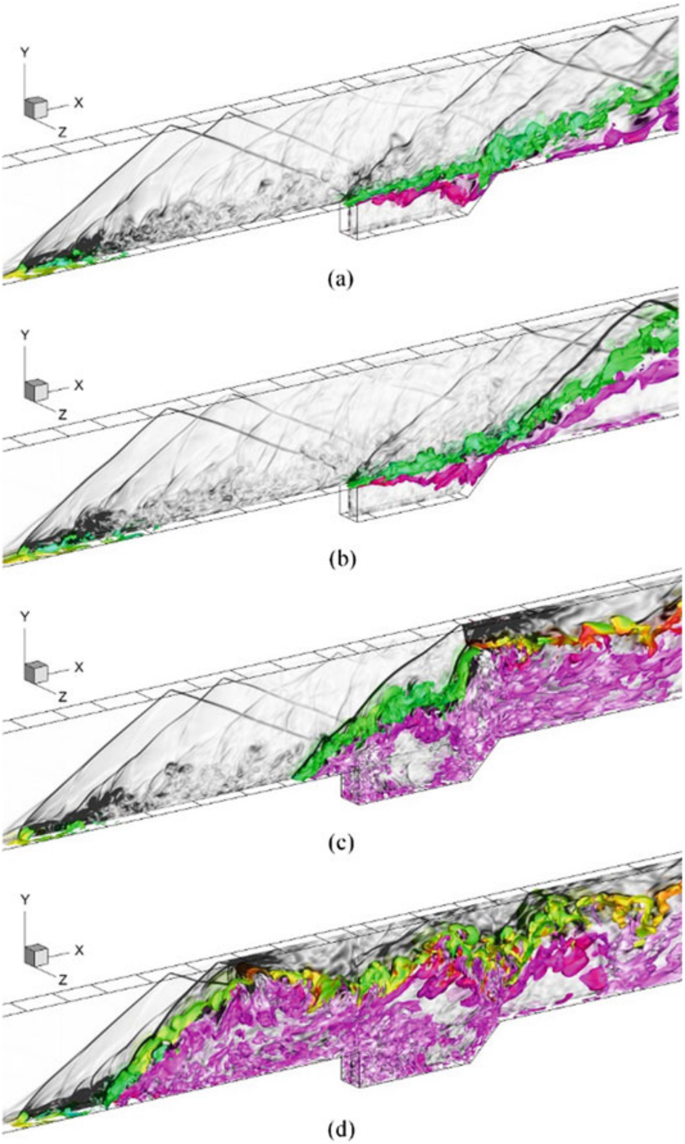

Fig. 5.55 Isolation surfaces of heat release rate, coloured with temperature and density gradients in the centre section for case 4 ($\Delta t = 50 \times D/U_\infty$) [33]

and separated boundary-layer forms a thermal throat when the flame spreads to the cavity position and further to accelerate the flame front, inducing flame flashback phenomenon.

Figures 5.56 and 5.57 illustrate the X-axial slices for the instantaneous temperature contours and the isolation surface of the $\lambda_2 = -0.1$ vortex structure. Initially, the flames are distributed in the jet-with-cavity shear layer and downstream of the cavity, where the subsonic region is located. During the flame flashback process, the flames gradually close even over to the sonic line. It is obvious that a thermal throat accompanied with intense combustion accelerates the flame front to propagate forward. It is apparent from Fig. 5.57 that the hairpin-like vortices near the injectors tense and fracture when they spread to downstream of the cavity, where the subsonic

Fig. 5.56 Oblique views of axial slices for instantaneous temperature contours for case 4 (blue line: stochiometric equivalent ratio; black line: sonic line; pink line: stagnation line for flow speed $\Delta t = 50 \times D/U_\infty$) [33]

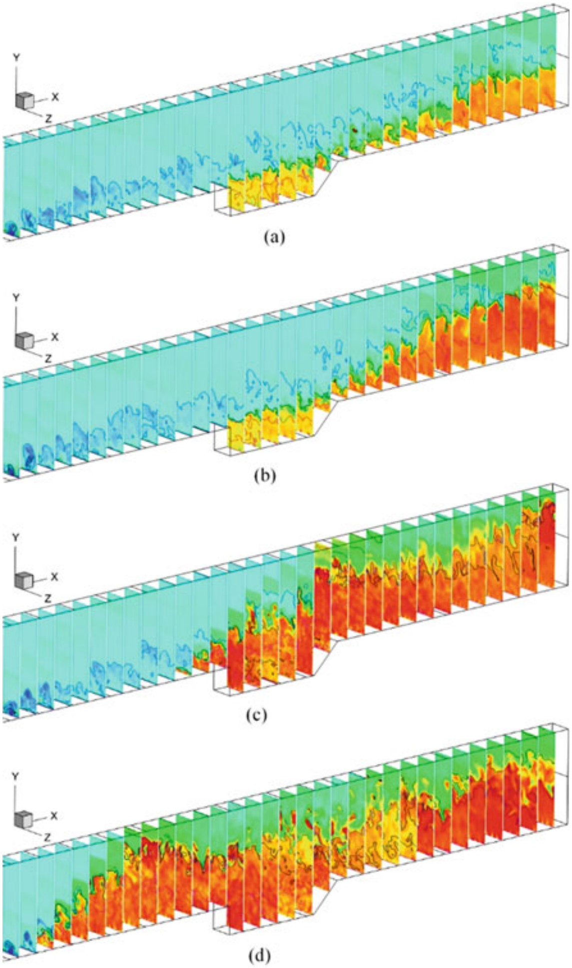

Fig. 5.57 Isolation surface of $\lambda_2 = -0.1$ vortex structure coloured with temperature for case 4 ($\Delta t = 50 \times D/U_\infty$) [33]

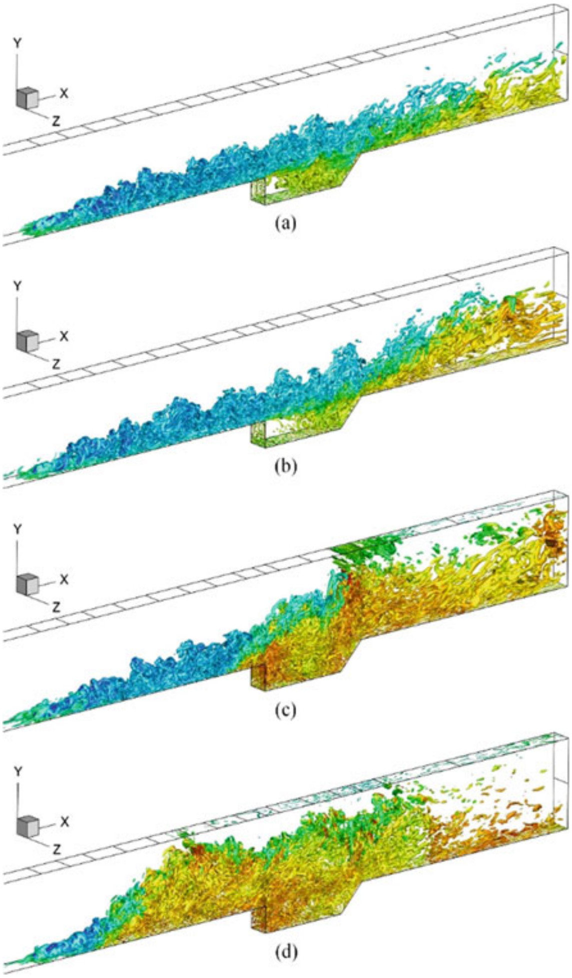

combustion zone is located. The flame flashback phenomenon is a development process of the energy accumulation. During the reaction procedure, the vortices coloured with high temperatures move forward against the flow. The separation zone gradually increases.

As suggested by Bilger [48], we define a mixture fraction to further evaluate the flame index factor, which is derived from C, H, and O elements are as follows

$$Z = \frac{2\left(Y_C - Y_{C,2}\right)/M_C + \left(Y_H - Y_{H,2}\right)/M_H - \left(Y_O - Y_{O,2}\right)/M_O}{2\left(Y_{C,1} - Y_{C,2}\right)/M_C + \left(Y_{H,1} - Y_{H,2}\right)/M_H - \left(Y_{O,1} - Y_{O,2}\right)/M_O}. \tag{5.3}$$

where Y_j and M_j are the elemental mass fractions and atomic masses for the elements carbon, hydrogen and oxygen and the subscripts 1 and 2 refer to values in the fuel and air streams, respectively.

The flame index factor can be defined by combining the mixture fraction and component gradient:

$$I = \frac{Z - Z_{st}}{|Z - Z_{st}|}\frac{1}{2}\left(1 + \frac{\nabla Y_{C_2H_4} \cdot \nabla Y_{O_2}}{\left|\nabla Y_{C_2H_4} \cdot \nabla Y_{O_2}\right|}\right), \tag{5.4}$$

where Z_{st} represents the mixture fraction at the stoichiometric equivalent ratio. From the flame index factor defined by Eq. (5.3), it is apparent that the combustion pattern can be divided into three categories in the combustion process. For fuel-rich premixed combustion, $Z - Z_{st} > 0$, $I_{rich} = 1$. For fuel-lean premixed combustion, $Z - Z_{st} < 0$, $I_{lean} = -1$. For diffusion combustion, $I_{diffusion} = 0$.

The change in the combustion mode in case 4 can be studied using the flame index factor. Figure 5.58 shows the development of the initial flame kernel inside the cavity. The red, yellow and brown areas denote the fuel-rich premixed, the diffusion

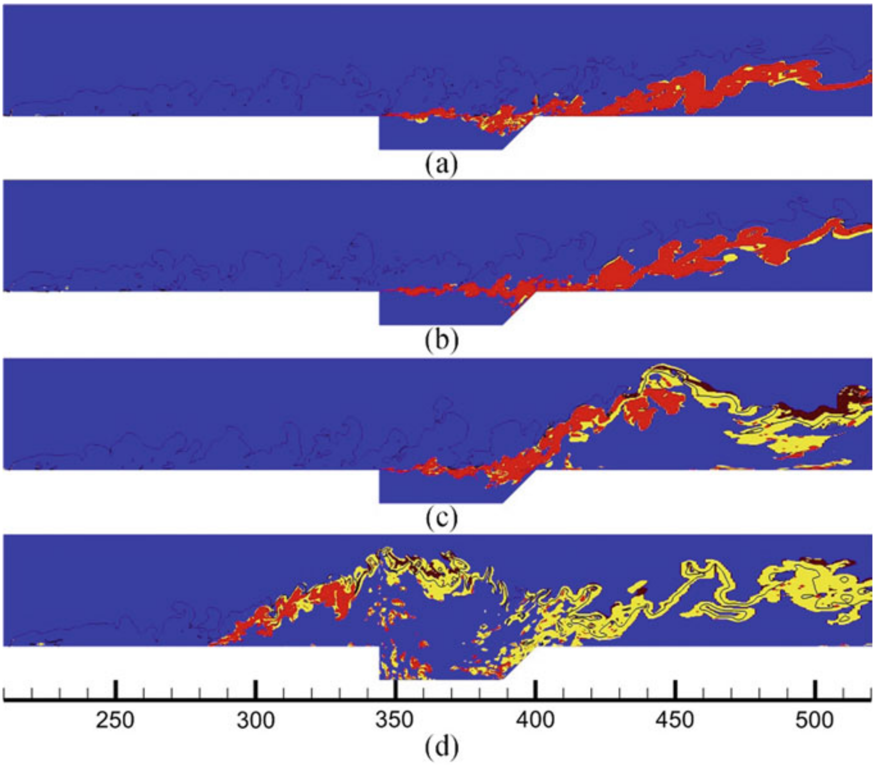

Fig. 5.58 Development of combustion modes for case 4 ($\Delta t = 50 \times D/U_\infty$) [33]

the fuel-lean premixed combustion zones, respectively. The black line denotes the stoichiometric line. Initially, most areas in the cavity and the jet-with-cavity shear layer are located in the fuel-rich premixed combustion zone. The flame downstream of the cavity mainly exhibits the forms of a fuel-rich premixed environment. The flame front spreads near the wall and the flame exhibits a fuel-rich premixed combustion mode. However, the flame located in the shear layer close to the main flow, rapidly changes into the diffusion combustion mode. The flame located in the fuel-rich premixed environment continues to react with the inflowing air, thus the diffusion combustion zone is formed. Additionally, the diffusion combustion zone unceasingly expands, where the vortex structure changes drastically. The entrainment effect can change the fuel or air gradient, which affects the distribution of the lean premixed combustion near the diffusion combustion area.

To quantitatively investigate the experimental and numerical calculation of the flame flashback speeds, a combustion iso-luminosity contour is used to characterise the combustion zone outlines for each flame image. The instantaneous speed of the flame front relative to the wall of the combustion chamber can be calculated using the change of the flame front position and the corresponding time interval. Figure 5.59 shows the combustion distribution at three different times.

Pressure distribution in the X-axial direction is obtained using pressure transducers installed along the centreline of the combustor lower walls. The measured averaged pressure distribution when flame front propagates to the injectors is presented in Fig. 5.60. Compared with the experimental results, the numerical curve of instan-

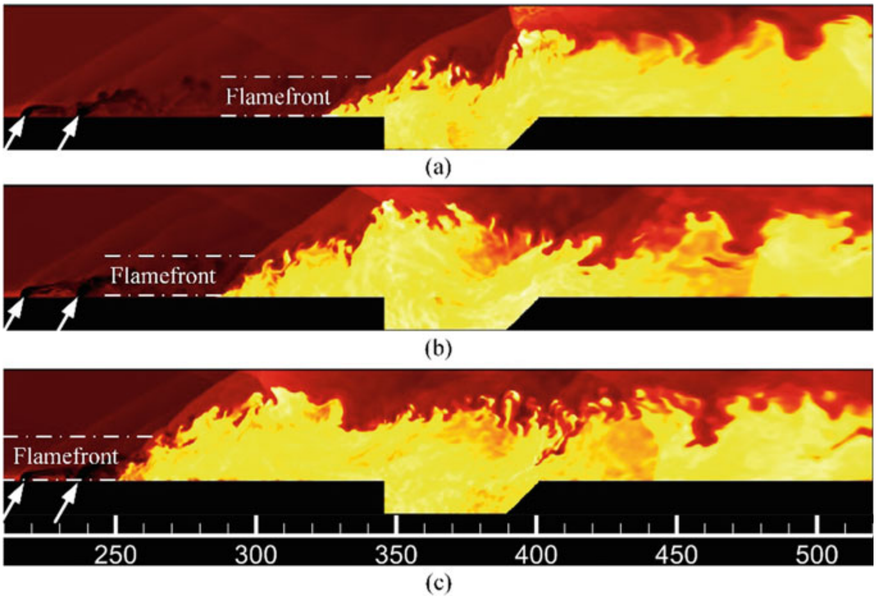

Fig. 5.59 Flame images at three different times with a consistent time step ($\Delta t = 15 \times D/U_{\infty}$) [33]

Fig. 5.60 Experimental and numerical dimensionless wall pressure on lower wall [33]

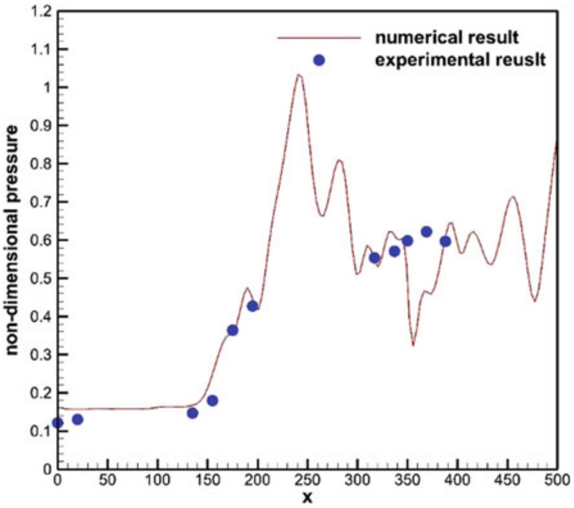

taneous pressure which is smoothed by Tecplot shows relatively good agreements, indicating the reliability of numerical method. The curves succeed to accurately predict the wall pressure upstream of the injectors. The heat-release causes a sharp rise of pressure upstream of the primary injectors. The pressure reaches a plateau in the cavity and rises again due to compression on the ramp wall of the cavity. Because of accumulated energy from the intense heat release, the pressure peak of flame front is slightly higher. These differences further demonstrate that the pressure fluctuations are strongly correlated with the flame flashback.

A series of schematic images are provided in Fig. 5.61 that show the flame flashback process based on the previous analysis in this paper. In typical cavity shear-layer stabilized combustion mode, the flame is anchored in the cavity shear layer, and the main combustion zone is also confined within the shear layer. The strong interactions between flame and boundary-layer greatly enhance the reaction. Then, the combustion fiercely heats the boundary layer downstream of the cavity, which leads to the present of the separated recirculation zone and compresses the bulk flow. In turn, the formed thermal throat induces the flame flashback phenomenon.

5.2.3 Theoretical Analyses

5.2.3.1 Mechanism of Flame Flashback

A simplified combustion opening system model is constructed (Fig. 5.62) based on the following assumptions:

1. The control volume is a tube, open at both ends, and the outer wall of the fluid container is adiabatic. V is the volume and L is the length.

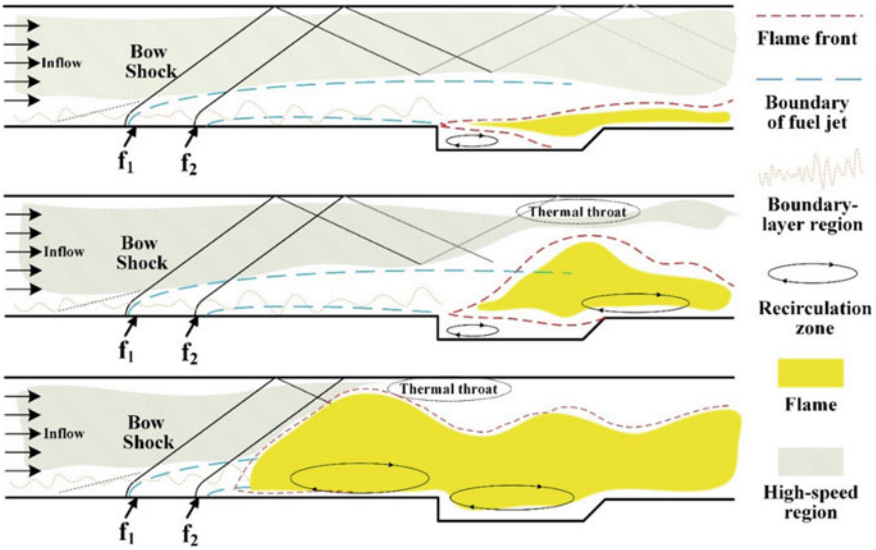

Fig. 5.61 Schematics of flame flashback from the cavity to the injectors for case 4 [33]

Fig. 5.62 Control volume for theoretical analysis

2. The initial temperature is T_0, the initial molarity of the premixed gases is C_0, and the mass flow rate is q (kg/s).
3. The temperature of the control volume rises to T, and the molarity of the premixed gases drops to C after the time period of δ_t. The temperature of the control volumes T and the molarity of the premixed gases C are equal throughout the control volume.
4. There is an n-order reaction model in the control volume.

The energy balance equation is expressed as:

$$\rho V c_p \frac{dT}{dt} = (\Delta H) V C^n k_0 \exp\left(-\frac{E}{RT}\right) - q c_p (T - T_0) \tag{5.5}$$

where ΔH denotes the reaction heat. k_0 and E denote the rate constant and activation energy in Arrhenius equation. The mass balance equation is given as:

$$\frac{dC}{dt} = C^n k_0 \exp\left(-\frac{E}{RT}\right) - \frac{q}{V\rho}(C_0 - C) \tag{5.6}$$

The heat released by the premixed gases in the control volume are used to heat the gases and are released from the system. The product generation is equal to the consumption of the premixed gases. So, the Eqs. (5.4) and (5.5) can be written by:

$$(\Delta H) V C^n k_0 \exp\left(-\frac{E}{RT}\right) = q c_p (T - T_0) \tag{5.7}$$

$$C^n k_0 \exp\left(-\frac{E}{RT}\right) = \frac{q}{V\rho}(C_0 - C) \tag{5.8}$$

Define the dimensionless number: dimensionless heat release rate $\varepsilon_1 = (C_0 - C)/C_0$ refers to the portion of the chemical energy in the premixed combustible gas that has been converted to heat divide the chemical energy that the entire premixed gas has in a unit volume; dimensionless heat dissipation rate $\varepsilon_2 = \left(\rho c_p (T - T_0)\right)/q C_0$ refers to the portion of heat carried out of the product by the product (the portion of the reaction heat used to heat up the product) divide the chemical energy of the entire premixed gas in a unit volume; The dimensionless action time $(\tau_d = \tau_1/\tau_2 = \left(\rho V k_0 C^{n-1}\right)/q)$. Where $\tau_1 = L/v = (\rho V)/q$ is premixed gas residence time in the control volume, and $\tau_2 = 1/\left(k_0 C^{n-1}\right)$ is the time which is required for completely chemical reaction of premixed gas; The dimensionless temperature $\theta = (RT)/E$; and dimensionless total heat release value $\psi = (\Delta H R C_0)/\left(\rho c_p E\right)$. The five dimensionless parameters are inserted into Eqs. (5.6) and (5.7), and the equations are then rearranged to yield

$$\varepsilon_1 = \frac{1}{1 + \frac{\exp\left(\frac{1}{\theta}\right)}{\tau_d}} \tag{5.9}$$

$$\varepsilon_2 = \frac{1}{\psi}(\theta - \theta_0) \tag{5.10}$$

For the purposes of discussion, typical values are obtained using the weighted average method: $C_0 = 0.005$, $\Delta H = 10000$, $E = 80000$, $\rho = 0.7$, $c_p = 2.0$, $T_0 = 1150$, and $\tau_d = 1.2$. τ_2 is calculated using a software package (CHEMKIN [44]).

Figure 5.63 shows that the straight line representing ε_2 cuts the curve representing ε_1 at two points. The lower point is the stable point of combustion, while the upper point is the threshold value for flame flashback. The combined effects of dimensionless heat release and heat dissipation affect the system stability and forms the thermal fluctuation. When the temperature fluctuates over the upper point, the heat release continuously exceeds the heat dissipation and the system temperature cannot self-stabilise. After this stage, the combustion increases widely and the flame in the

Fig. 5.63 Dimensionless heat release rate ε_1 and heat dissipation rate ε_2 as functions of dimensionless temperature θ [33]

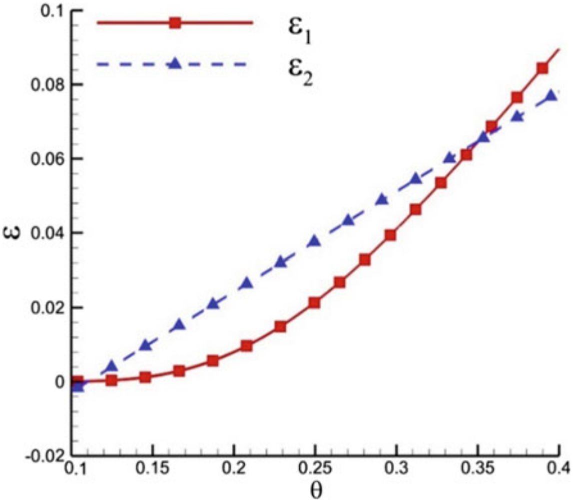

separated boundary-layer spreads into the mainstream, forming a thermal throat and further trigger flame flashback.

Figures 5.64, 5.65, and 5.66 show ε as a function of θ under different conditions. For brief discussion, the x-axis is converted to temperature in following figures. Figure 5.64 shows the effect of the dimensionless initial temperature on dimensionless heat dissipation rate. When the initial dimensionless temperature increases from θ_{01} to θ_{02}, the dimensionless heat dissipation rate ε_2 decreases, leading to the temperature fluctuation threshold decrease. For case 1, due to additional turbulent boundary-layer, the increased compression effect enhances the initial temperature. Hence, the flame flashback phenomenon can be easily triggered under the reduced

Fig. 5.64 The effect of dimensionless initial temperature on dimensionless heat dissipation rate [33]

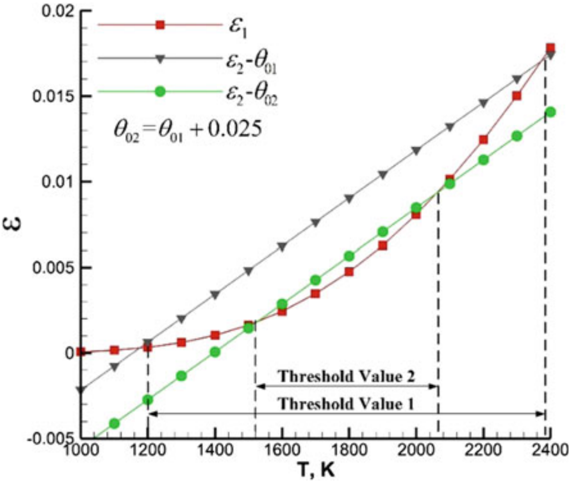

Fig. 5.65 The effect of dimensionless action time on dimensionless heat release rate [33]

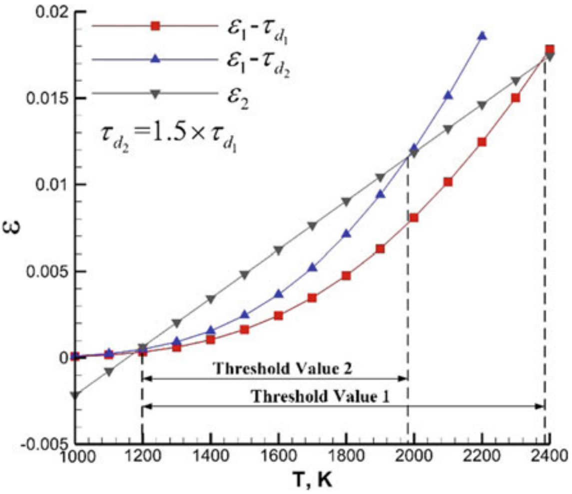

Fig. 5.66 The effect of dimensionless total heat release value on dimensionless heat dissipation rate [33]

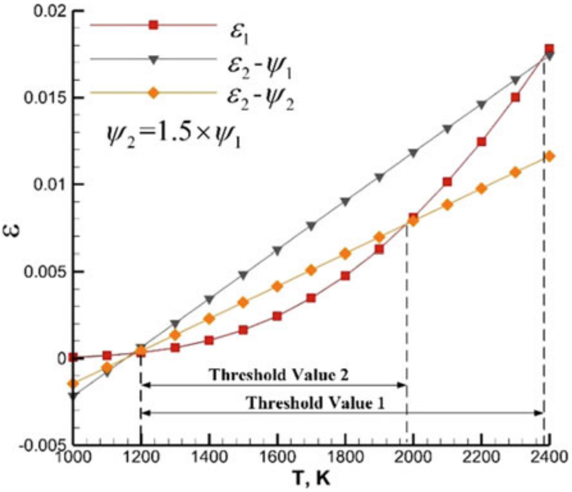

temperature fluctuation threshold condition. For case 4, additional thermal disturbance downstream of the cavity increases the temperature fluctuation range. Hence, the fluctuating temperature can easily exceed the upper unstable point, inducing the flame flashback phenomenon.

Figure 5.65 shows the effect of the dimensionless action time on dimensionless heat release rate. The added thermal disturbance in cases 3 and 4 interacting with flame downstream of cavity can prompt boundary layer separation and compressing the bulk flow. This compression effect increases the dimensionless action time of flame which acts on the dimensionless residence time of fuel τ_d. Increasing the dimensionless action time enhances the heat release rate and reduces the temperature fluctuation threshold. Although the energy of the thermal disturbance in case 3 is larger than case 4, the patched high temperature close to outflow is rapidly blown out of the flow channel. The residence time of the disturbance is too short to trigger flame flashback phenomenon.

Figure 5.66 shows the effect of the dimensionless heat value on dimensionless heat dissipation rate. Generally, the improvement of local fuel mixing can change dimensionless total heat release value. For case 5, the amplified diffusion coefficient improves the mixing efficiency at the boundary-layer surface between fuel and air, further decrease temperature threshold value. In addition, the appropriate local equivalence ratio can enhance combustion greatly, increasing the temperature fluctuation range.

5.2.3.2 One Dimensional Analysis in the Competition of Auto-ignition and Flame Propagation

To identify the auto-ignition issue under such high total temperature, the one-dimensional analysis method is introduced in this section. Figure 5.67 shows the streamwise distributions of pressure, temperature and velocity from different longitudinal positions at a certain time instant. The heat release within the flame region can substantially increase the temperature and pressure, compressing the incoming flow and generating shock waves. As the compressing effects spread upstream, temperature and pressure are raised, and velocity is decreased. Near the lower wall, the pressure and temperature rise after the injection (x = 215 mm, x = 235 mm) due to bow shock wave. The abrupt changes are caused by the oblique shock wave. For velocity, the low speed separation and back flow regions appear near lower wall. The velocity in main flow is closer to inflow speed.

As shown in Fig. 5.68, auto-ignition delay times under different temperature and pressure is estimated by CHEMKIN [44] using the seven species and three steps M_2 ethylene/air chemical kinetic mechanism. The auto-ignition delay time rapidly decreases from ~10^{-2} s at 1000 K to ~10^{-5} s at 1800 K, indicating that the auto-ignition behaviour is sensitive to the change of temperature in the range of 1000–1800 K.

To estimate the ignition (flame front) position, as Knop et al. [49] and Colin et al. [50] did, tabulation of auto-ignition delay times based on local pressure and temperature is presented. By defining the rate of auto-ignition progress φ, the auto-ignition delay distance is provided with the local pressure, temperature and velocity data. The auto-ignition delay position x_a is

$$x_a = \int_0^1 \tau_a(x) \cdot \upsilon(x) d\varphi \tag{5.11}$$

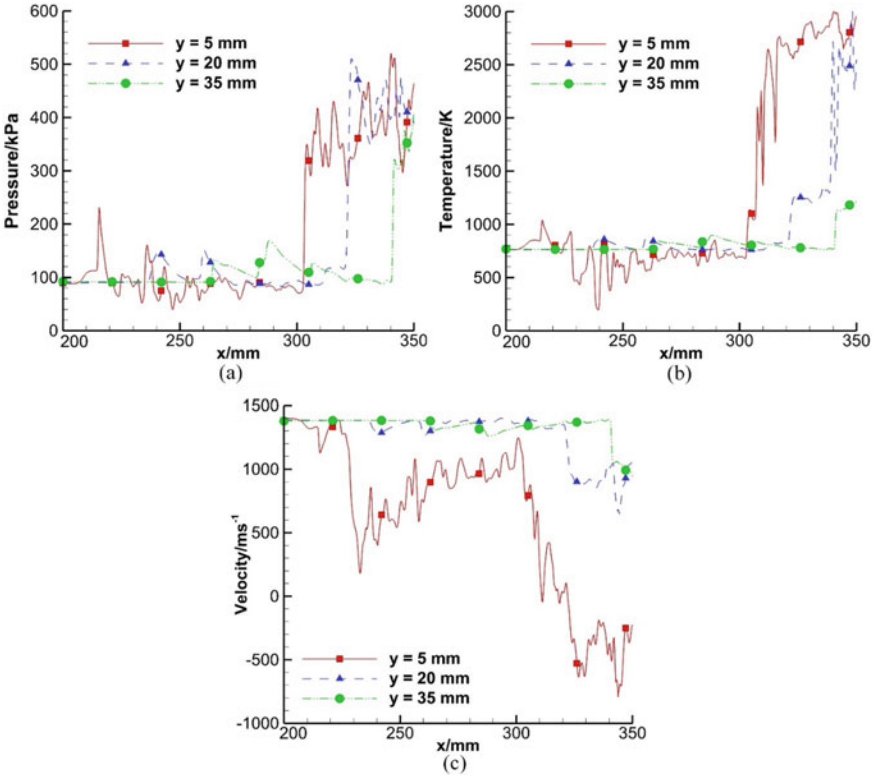

(a)

(b)

(c)

Fig. 5.67 Streamwise distribution of flow parameters at a certain time instant [33]

Fig. 5.68 Auto-ignition delay time [33]

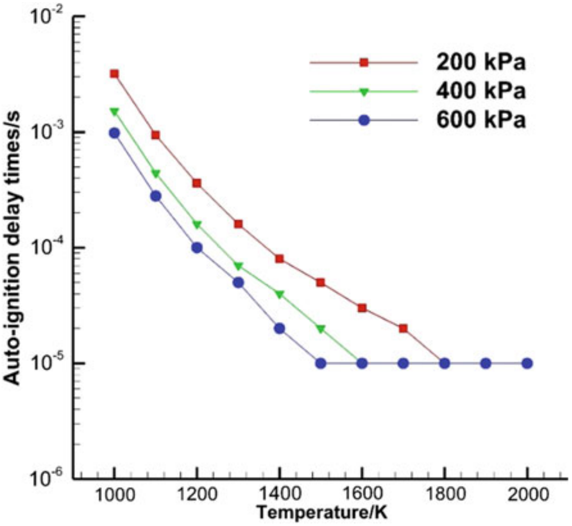

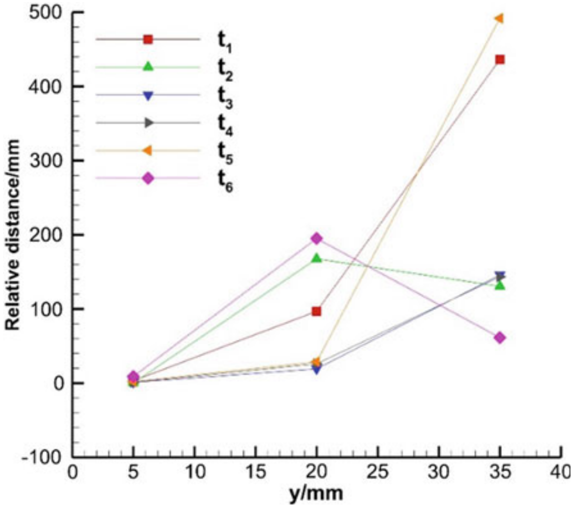

Fig. 5.69 relative distance between auto-ignition position and flame front position at different instantaneous [33]

$\tau_a(x)$ is the local ignition delay time calculated by tabulation of pressure and temperature at point x. $\upsilon(x)$ is the local velocity. The auto-ignition is accomplished and a flame appears when $\varphi = 1$. The integral started at x = 200 mm position, as auto-ignition occurs when the fuel and hot air are mixed. The relative distance (x_r) between auto-ignition position and flame front position x_f is defined

$$x_r = x_a - x_f \tag{5.12}$$

As shown in Fig. 5.69, the estimated relative distances are positive, indicating that the auto-ignition position is located in downstream region of flame front. It can be demonstrated that there are no auto-ignition issues for ethylene under this condition.

5.3 Summary

Flame flashback phenomenon inside an ethylene-fueled scramjet combustor is experimentally investigated in Mach 2.1 facility which simulates Mach 4 flight condition. Experimental and numerical investigations of flame flashback phenomenon have been carried out inside an ethylene-fueled scramjet combustor with a cavity flameholder under the condition of flight Mach 5.5. Some results exhibit quasi-periodic combustion oscillation in the combustion chamber.

1. The experimental results exhibit some factors can separate the boundary layer. The interaction between combustion and separated boundary layer forms a thermal throat which induces thermal chocking, thus induce the flame flashback phenomenon.

2. The flashback develops explosively from the cavity pilot flame at regular intervals. Analysis of the experimental data suggests that the flame flashback is related to flame acceleration similar to deflagration-to-detonation transition.
3. Factors like higher fuel equivalence ratio, sharper injection angle, longer premixing distance, multi-jets, the higher cavity length-to-depth ratio, sharper cavity aft ramp angle, the closer air throttling can induce flame flashback phenomenon. The flame front distributions, flame propagation speeds and quasi-periodic oscillation frequencies obtained by the iso-luminosity contour method shows significant differences in different cases.
4. The centralized injection scheme will result in combustion oscillation in scramjet combustor whose period and intensity will increase as the premixing distance becomes longer. It has been confirmed that distributed injection scheme is an effective method to avoid the combustion oscillation in scramjet combustor, which can induce two parts interacting stable flame.
5. In addition, a simplified combustion opening sys-tem model has been established to analyse combustion oscillation mechanisms, which theoretically demonstrates that above factors can destroy the balance of heat release and dissipation, causing the system cannot self-stabilise once certain temperature fluctuation thresholds in sensitive areas are exceeded. At the same time, the auto-ignition model excludes the possibility of flame flashback generated by auto-ignition effect.

References

1. Wang, H. B., et al. (2015). Mixing-related low frequency oscillation of combustion in an ethylene-fueled supersonic combustor. *Proceedings of the Combustion Institute, 35*(2), 2137–2144.
2. Sun, M. B., et al. (2015). Flame flashback in a supersonic combustor fueled by ethylene with cavity flameholder. *Journal of Propulsion and Power, 31*(3), 976–981.
3. Bychkov, V., et al. (2012). Gas compression moderates flame acceleration in deflagration-to-detonation transition. *Combustion Science and Technology, 184*(7–8), 1066–1079.
4. Valiev, D. M., et al. (2009). Different stages of flame acceleration from slow burning to Chapman-Jouguet deflagration. *Physical Review E, 80*(3), 036317.
5. Dorofeev, S. B. (2011). Flame acceleration and explosion safety applications. *Proceedings of the Combustion Institute, 33*(2), 2161–2175.
6. Ouyang, H., Liu, W., & Sun, M. (2016). Parametric study of combustion oscillation in a single-side expansion scramjet combustor. *Acta Astronautica, 127,* 603–613.
7. Sun, M. B., et al. (2014). Experimental investigation of supersonic model combustor with distributed injection of supercritical kerosene. *Journal of Propulsion and Power, 30*(6), 1537–1542.
8. Fotia, M. L., & Driscoll, J. F. (2013). Ram-scram transition and flame/shock-train interactions in a model scramjet experiment. *Journal of Propulsion and Power, 29*(1), 261–273.
9. Karl, S., et al. (2012). Cfd analysis of unsteady combustion phenomena in the hyshot-ii scramjet configuration. In *18th AIAA/3AF International Space Planes and Hypersonic Systems and Technologies Conference* (p. 5912). AIAA.
10. Larsson, J., et al. (2015). Incipient thermal choking and stable shock-train formation in the heat-release region of a scramjet combustor. Part II: Large eddy simulations. *Combustion and Flame, 162*(4), 907–920.

11. Laurence, S., et al. (2012). Investigation of unsteady/quasi-steady scramjet behavior using high-speed visualization techniques. In *18th AIAA/3AF International Space Planes and Hypersonic Systems and Technologies Conference* (p. 5913). AIAA.
12. Laurence, S., et al. (2011). An experimental investigation of steady and unsteady combustion phenomena in the HyShot II combustor. In *17th AIAA International Space Planes and Hypersonic Systems and Technologies Conference* (p. 2310). AIAA.
13. Laurence, S. J., et al. (2013). Transient fluid-combustion phenomena in a model scramjet. *Journal of Fluid Mechanics, 722,* 85–120.
14. Frost, M. A., et al. (2009). Boundary-layer separation due to combustion-induced pressure rise in a supersonic flow. *AIAA Journal, 47*(4), 1050–1053.
15. Mathur, T., et al. (2001). Supersonic combustion experiments with a cavity-based fuel injector. *Journal of Propulsion and Power, 17*(6), 1305–1312.
16. O'Byrne, S., et al. (2012). *OH PLIF imaging of supersonic combustion using cavity injection*.
17. Ouyang, H., Liu, W., & Sun, M. (2014). Numerical investigation of the influence of injection scheme on the ethylene supersonic combustion. *Advances in Mechanical Engineering, 6,* 124204.
18. Wang, H. B., Wang, Z. G., & Sun, M. B. (2013). Experimental study of oscillations in a scramjet combustor with cavity flameholders. *Experimental Thermal and Fluid Science, 45,* 259–263.
19. Wang, Z. G., et al. (2015). Mixing-related low frequency oscillation of combustion in an ethylene-fueled supersonic combustor. *Proceedings of the Combustion Institute, 35,* 2137–2144.
20. Hu, Z. M., et al. (2008). Numerical study of the oscillations induced by shock/shock interaction in hypersonic double-wedge flows. *Shock Waves, 18*(1), 41.
21. Zhao, G. Y., et al. (2018). Investigations of injection parameters on combustion oscillation in a supersonic crossflow. *Acta Astronautica, 152,* 426–436.
22. Laurence, S. J., et al. (2015). Incipient thermal choking and stable shock-train formation in the heat-release region of a scramjet combustor. Part I: Shock-tunnel experiments. *Combustion and Flame, 162*(4), 921–931.
23. Micka, D. J. (2010). *Combustion stabilization, structure, and spreading in a laboratory dual-mode scramjet combustor*. The University of Michigan.
24. Ali, M., & Islam, A. K. M. S. (2006). Study on main flow and fuel injector configurations for Scramjet applications. *International Journal of Heat and Mass Transfer, 49*(19), 3634–3644.
25. Pudsey, A. S., & Boyce, R. R. (2010). Numerical investigation of transverse jets through multiport injector arrays in a supersonic crossflow. *Journal of Propulsion and Power, 26*(6), 1225–1236.
26. Zhao, G. Y., et al. (2019). Experimental investigations of cavity parameters leading to combustion oscillation in a supersonic crossflow. *Acta Astronautica, 155,* 255–263.
27. Sun, M. B., et al. (2011). Parametric study on self-sustained oscillation characteristics of cavity flameholders in supersonic flows. *Proceedings of the Institution of Mechanical Engineers, Part G: Journal of Aerospace Engineering, 225*(6), 597–618.
28. Zare Behtash, H., et al. (2015). Transverse jet-cavity interactions with the influence of an impinging shock. *International Journal of Heat and Fluid Flow, 53,* 146–155.
29. Babinsky, H., & Harvey, J. K. (2011). *Shock wave-boundary-layer interactions* (Vol. 32). Cambridge University Press.
30. Tian, Y., et al. (2017). Investigation of combustion process of a kerosene fueled combustor with air throttling. *Combustion and Flame, 179,* 74–85.
31. Jiang, G. S., & Shu, C. W. (1996). Efficient implementation of weighted ENO schemes. *Journal of Computational Physics, 126,* 202–228.
32. Wang, H. B., et al. (2014). Numerical study on supersonic mixing and combustion with hydrogen injection upstream of a cavity flameholder. *Heat Mass Transfer, 50,* 211–223.
33. Zhao, G. Y., et al. (2019). Investigation of flame flashback phenomenon in a supersonic crossflow with ethylene injection upstream of cavity flameholder. *Aerospace Science and Technology, 87,* 190–206.

34. Wang, H. B., et al. (2013). Combustion characteristics in a supersonic combustor with hydrogen injection upstream of cavity flameholder. *Proceedings of the Combustion Institute, 34,* 2073–2082.
35. Wang, H. B., et al. (2013). Large-Eddy/Reynolds-averaged Navier-Stokes simulation of combustion oscillations in a cavity-based supersonic combustor. *Internationl Journal of Hydrogen Energy, 38,* 5918–5927.
36. Spalart, P. R., & Allmaras, S. R. (1992). A one-equation turbulence model for aerodynamic flows. In *30th Aerospace Sciences Meeting & Exhibit* (p. 439). Reno, NV: AIAA.
37. Yoshizawa, A., & Horiuti, K. (1985). A statistically-derived subgrid-scale kinetic energy model for the large-Eddy simulation of turbulent flows. *Journal of the Physical Society of Japan, 54*(8), 2834–2839.
38. Wang, H., et al. (2011). A hybrid LES (Large Eddy Simulation)/assumed sub-grid PDF (Probability Density Function) model for supersonic turbulent combustion. *Science China Technological Sciences, 54*(10), 2694.
39. Lund, T. S., Wu, X., & Squires, K. D. (1998). Generation of turbulent inflow data for spatially-developing boundary layer simulations. *Journal of Computational Physics, 140*(2), 233–258.
40. Liu, K., & Pletcher, R. H. (2006). Inflow conditions for the large Eddy simulation of turbulent boundary layers: a dynamic recycling procedure. *Journal of Computational Physics, 219*(1), 1–6.
41. Xiao, X., et al. (2003). Inflow boundary conditions for hybrid large Eddy/Reynolds averaged Navier-Stokes simulations. *AIAA Journal, 41*(8), 1481–1489.
42. Urbin, G., & Knight, D. (2001). Large-Eddy simulation of a supersonic boundary layer using an unstructured grid. *AIAA Journal, 39*(7), 1288–1295.
43. Brindle, A., Boyce, R. R., & Neely, A. J. (2005). CFD analysis of an ethylene-fueled intake-injection shock-induced-combustion scramjet configuration. In *AIAA/CIRA 13th International Space Planes and Hypersonics Systems and Technologies Conference* (p. 3239). Capua, Italy: AIAA.
44. Xu, C., & Konnov, A. A. (2012). Validation and analysis of detailed kinetic models for ethylene combustion. *Energy, 43*(1), 19–29.
45. Kalitan, D. M., Hall, J. M., & Petersen, E. L. (2005). Ignition and oxidation of ethylene-oxygen-diluent mixtures with and without silane. *Journal of Propulsion and Power, 21*(6), 1045–1056.
46. Baker, J. A., & Skinner, G. B. (1972). Shock-tube studies on the ignition of ethylene-oxygen-argon mixtures. *Combustion and Flame, 19,* 347–350.
47. Konnov, A. A. (2009). Implementation of the NCN pathway of prompt-NO formation in the detailed reaction mechanism. *Combustion and Flame, 156,* 2093–2105.
48. Bilger, R. W. (1980). Turbulent flows with nonpremixed reactants. In P. A. Libby & F. A. Williams (Eds.), *Turbulent reacting flows* (pp. 65–113) Berlin, Heidelberg: Springer.
49. Knop, V., Michel, J.-B., & Colin, O. (2011). On the use of a tabulation approach to model auto-ignition during flame propagation in SI engines. *Applied Energy, 88*(12), 4968–4979.
50. Colin, O., Pires da Cruz, A., & Jay, S. (2005). Detailed chemistry-based auto-ignition model including low temperature phenomena applied to 3-D engine calculations. *Proceedings of the Combustion Institute, 30*(2), 2649–2656.